

# **FY20 SAM Code Developments and Validations for Transient Safety Analysis of Advanced non-LWRs**

---

**Nuclear Science and Engineering Division**

### **About Argonne National Laboratory**

Argonne is a U.S. Department of Energy laboratory managed by UChicago Argonne, LLC under contract DE-AC02-06CH11357. The Laboratory's main facility is outside Chicago, at 9700 South Cass Avenue, Argonne, Illinois 60439. For information about Argonne and its pioneering science and technology programs, see [www.anl.gov](http://www.anl.gov).

### **DOCUMENT AVAILABILITY**

**Online Access:** U.S. Department of Energy (DOE) reports produced after 1991 and a growing number of pre-1991 documents are available free at OSTI.GOV (<http://www.osti.gov/>), a service of the US Dept. of Energy's Office of Scientific and Technical Information.

### **Reports not in digital format may be purchased by the public from the National Technical Information Service (NTIS):**

U.S. Department of Commerce  
National Technical Information Service  
5301 Shawnee Rd  
Alexandria, VA 22312  
**[www.ntis.gov](http://www.ntis.gov)**  
Phone: (800) 553-NTIS (6847) or (703) 605-6000  
Fax: (703) 605-6900  
Email: **[orders@ntis.gov](mailto:orders@ntis.gov)**

### **Reports not in digital format are available to DOE and DOE contractors from the Office of Scientific and Technical Information (OSTI):**

U.S. Department of Energy  
Office of Scientific and Technical Information  
P.O. Box 62  
Oak Ridge, TN 37831-0062  
**[www.osti.gov](http://www.osti.gov)**  
Phone: (865) 576-8401  
Fax: (865) 576-5728  
Email: **[reports@osti.gov](mailto:reports@osti.gov)**

### **Disclaimer**

This report was prepared as an account of work sponsored by an agency of the United States Government. Neither the United States Government nor any agency thereof, nor UChicago Argonne, LLC, nor any of their employees or officers, makes any warranty, express or implied, or assumes any legal liability or responsibility for the accuracy, completeness, or usefulness of any information, apparatus, product, or process disclosed, or represents that its use would not infringe privately owned rights. Reference herein to any specific commercial product, process, or service by trade name, trademark, manufacturer, or otherwise, does not necessarily constitute or imply its endorsement, recommendation, or favoring by the United States Government or any agency thereof. The views and opinions of document authors expressed herein do not necessarily state or reflect those of the United States Government or any agency thereof, Argonne National Laboratory, or UChicago Argonne, LLC.

# **FY20 SAM Code Developments and Validations for Transient Safety Analysis of Advanced non-LWRs**

---

prepared by  
R. Hu, G. Hu, L. Zou, A. Klingberg, T. Fei, D. Nunez  
Nuclear Science and Engineering Division, Argonne National Laboratory

September 2020



## EXECUTIVE SUMMARY

The System Analysis Module (SAM) is under development at Argonne National Laboratory as a modern system-level modeling and simulation tool for advanced non-light water reactor safety analyses. It utilizes the object-oriented application framework MOOSE to leverage the modern software environment and advanced numerical methods. The capabilities of SAM are being extended to enable the transient modeling, analysis, and design of various advanced nuclear reactor systems. This report summarizes major progress in SAM code development, capability enhancements, demonstration, and validation to support transient safety analysis of advanced non-LWRs.

Rapid developments continued in fiscal year 2020 (FY20) to support various needs of the advanced reactor community, especially the NRC and industry on the licensing safety analysis of advanced reactor designs. Significant code changes were made to provide various capability enhancements, bug fixes, and user friendliness improvements. Major code updates are summarized in Section 1, while four important enhancements are detailed in Sections 2-5, including a multi-dimension flow model; reactivity feedback and decay heat models; control and trip system modeling, and additional fluid and solid thermophysical property models. Code validation activities in FY20 include using test data from the Fast Flux Test Facility (FFTF), the High Temperature Test Facility (HTTF), and several separate effects test facilities for pebble-bed modeling.



## Table of Contents

<b>EXECUTIVE SUMMARY .....</b>	<b>I</b>
<b>TABLE OF CONTENTS .....</b>	<b>III</b>
<b>LIST OF FIGURES .....</b>	<b>IV</b>
<b>LIST OF TABLES .....</b>	<b>IV</b>
<b>1 INTRODUCTION .....</b>	<b>1</b>
1.1 OVERVIEW OF CURRENT CAPABILITIES .....	2
<b>2 UPDATES IN MULTI-DIMENSIONAL FLOW MODELING .....</b>	<b>5</b>
<b>3 SAM ENHANCEMENTS IN REACTIVITY FEEDBACK AND DECAY HEAT MODELING.....</b>	<b>8</b>
3.1 FUEL AXIAL EXPANSION REACTIVITY FEEDBACK.....	8
3.2 DECAY HEAT IMPLEMENTATION IN SAM .....	11
<b>4 CONTROL AND TRIP SYSTEM MODELING .....</b>	<b>15</b>
4.1 GENERAL DESIGN FEATURE .....	15
4.2 TESTING.....	17
4.2.1 Case 1: component test.....	17
4.2.2 Case 2: Mass flow controller.....	19
4.2.3 Case 3: Reactivity controller.....	20
<b>5 FLUID AND SOLID PROPERTY MODEL UPDATES.....</b>	<b>22</b>
5.1 SALT PROPERTIES AND EQUATION-OF-STATE .....	22
5.1.1 Pure Salt Property Modeling.....	22
5.1.2 Mixed Salt Property Modeling.....	24
5.1.3 MSRE Fuel Property Modeling.....	25
5.2 LIQUID METAL PROPERTY MODELING.....	25
5.3 SOLID PROPERTIES .....	26
5.3.1 Clad Property Modeling.....	26
5.3.2 Fuel Property Modeling .....	27
<b>6 CODE VALIDATION EFFORTS .....</b>	<b>30</b>
6.1 CODE VALIDATION USING FFTF TEST DATA .....	30
6.2 CODE VALIDATION USING HTTF TEST DATA .....	30
6.3 CODE VALIDATION FOR PEBBLE BED MODELING .....	31
<b>ACKNOWLEDGEMENT.....</b>	<b>32</b>
<b>REFERENCE:.....</b>	<b>33</b>

## LIST OF FIGURES

Figure 1-1. Steady state solid temperature profile of a heat-pipe-cooled micro reactor. Horizontal cut view (left) and vertical cut view (right). .....	4
Figure 1-2. Transient average solid temperature of different blocks during an unprotected loss of heat sink event.....	4
Figure 2-1. The SUPERCANVA facility and flow directions.....	6
Figure 2-2. SAM results for case T1: Temperature time series at the inlet $T_{fi}$ , outlet $T_{fa}$ , and several y locations (along V2). The circles and solid lines represent the experimental data and the SAM results, respectively. Note that $T_{fi}$ is overlapping with $T_{fi}^*$ . .....	7
Figure 2-3. CFD, SAM, and experimental temperature profiles for cases P3 and P4 at locations a) V1 and b) V2. The circles and solid lines represent the experimental data and the CFD results, respectively. The dashed lines represent the SAM results. ....	7
Figure 3-1. Normalized fuel reactivity worth profile at different axial layers for the numerical tests. ....	10
Figure 3-2. Detailed time notation for decay heat modeling. ....	12
Figure 3-3. Test 3 decay heat from analytical and SAM solutions.....	14
Figure 3-4. Relative difference between the analytical and SAM solutions for Test 3. ....	14
Figure 4-1. Hierarchy of classes for control and trip system models. ....	16
Figure 4-3. Diagram for test case 1: component test. ....	18
Figure 4-4. Comparisons of outputs y1 and y2 for case 1: component test. ....	19
Figure 4-5. Comparisons of values of each component for case 1: component test.....	19
Figure 4-6. Diagram for test case 2: mass flow controller.....	20
Figure 4-7. Comparison of outlet temperature and specified temperature for test case 2: mass flow controller.....	20
Figure 4-8. Diagram for test case 3: reactivity controller. ....	21
Figure 4-9. Comparison of reactor fission power and specified power for test case 3: reactivity controller. ....	21

## LIST OF TABLES

Table 3-1: Comparison of SAM fuel axial expansion reactivity feedback models for solid fuel and liquid fuel. ....	11
Table 3-2: Description of notations used in equations.....	11
Table 4-1: Operations of control components .....	17
Table 4-2: Operations of trip components. ....	17
Table 4-3: Components in the test case 1. ....	18
Table 5-1: Constants Used in Heat Capacity Correlations for UO <sub>2</sub> and MOX. ....	27



## 1 Introduction

An advanced system analysis tool, SAM [1][2], is under development at Argonne National Laboratory for advanced non-LWR reactor safety analysis. It aims to provide fast-running, modest-fidelity, whole-plant transient analyses capabilities, which are essential for fast turnaround design scoping and engineering analyses of advanced reactor concepts. While SAM is being developed as a system-level modeling and simulation tool, advanced modeling techniques being implemented include a reduced-order three-dimensional module [3], pseudo 3-D conjugate heat transfer modeling in reactor core [4], flexible and multi-scale modeling of heat transfer between fluid and structures [5], in addition to the advances in software environments and design, and numerical methods.

SAM aims to be a generic system-level safety analysis tool for advanced non-LWRs, including Liquid-Metal-cooled fast Reactors (LMR), Molten Salt Reactors (MSR), Fluoride-salt-cooled High-temperature Reactors (FHR), and High-Temperature Gas-cooled Reactors (HTGR). SAM takes advantage of advances in physical modeling, numerical methods, and software engineering to enhance its user experience and usability. It utilizes an object-oriented computational framework (MOOSE [6]), and its underlying meshing and finite-element library and linear and non-linear solvers, to leverage the modern advanced software environments and numerical methods.

Rapid development continued in fiscal year 2020 (FY20) to support various needs of the advanced reactor community, especially the NRC and industry on the licensing safety analysis of advanced reactor designs. SAM is receiving increasing interests in the nuclear community for its use in advanced reactor design and safety analyses. Significant accomplishments in user engagements in FY20 include:

- Joint code development with Kairos Power for molten-salt-cooled pebble-bed reactors under the support of a Technology Commercialization Fund (TCF) award and a DOE-NE's industry FOA award.
- Provide technical support to NRC on SAM applications to advanced non-LWR safety analysis and improve code capabilities to close gaps in the safety modeling of various advanced reactor designs.
- Support reactor design analysis and assessment for HolosGen's gas-cooled micro reactor and Moltex's stable salt reactor concepts under the support of DOE ARPA-E's MEITNER program.
- SAM code licensees granted in FY20 include BWX Technologies, NuScale, Virginia Commonwealth University, University of Wisconsin, while the license agreement with Moltex Energy, TerraPower (updated license) are undergoing.

In FY 20, the SAM code has gone through significant changes with capability enhancements, bug fixing, and user friendliness improvements. The major updates include:

- Improvements in the reduced-order multi-dimensional flow model for thermal mixing and stratification in a large pool [7].
- Improvement in fuel axial expansion reactivity feedback modeling for liquid fuel.
- Implementation of decay heat modeling for stationary fuel.
- Design and implementation of control and trip system in SAM. A set of proportional–integral–derivative (PID) controllers and trip logic units are implemented.

- Significant improvements in salt freezing modeling for molten-salt-cooled reactors [8].
- A major bug fix of heat transfer coefficient calculations when switching different correlations due to flow condition changes. It greatly improved the robustness and performance of the code.
- Improvements in equation of state models, which removed the potential inconsistencies when users provide both specific heat and enthalpy models in the input.
- Additional fluid properties are implemented, including a set of pure salt, MSRE fuel salt, lead, LBE.
- A set of fuel and cladding material properties are implemented.
- A new valve component model is implemented.
- A set of postprocessors are implemented for checking mass and energy conservation in the system.
- Updates in heat structure boundary condition modeling to allow for SAM/TRACE coupling through BlueCRAB.
- Flexible and multi-scale modeling of heat transfer between fluid and structures, including coupled 1D fluid flow and 2D/3D heat structure or coupled 2D/3D flow with 2D/3D heat structure [9].

SAM also utilizes the application- and validation-driven code development approach. These demonstration and validations lead up to the continuous assessment of the code capabilities and performance for a wide range of advanced reactor applications. Code demonstration activities in FY20 cover simulations of a molten salt fast reactor [10], a molten-salt-cooled pebble-bed reactor [11], a gas-cooled micro reactor, and a stable salt reactor [12]. The demonstration simulations also resulted in reference plant models for these reactor types, which can be further utilized and tested by code users to examine the SAM code capabilities and identify capability gaps for these types of reactors. Code validation activities in FY20 include using test data from the Fast Flux Test Facility (FFTF), the High Temperature Test Facility (HTTF), and several separate effects test facilities for pebble-bed modeling.

This report summarizes the FY20 progress in SAM code development, capability enhancements, and validation to support transient safety analysis of advanced non-LWRs. This report is structured as follows: Section 2 provides a summary on the updated multi-dimensional flow model and its validation. Section 3 describes the recent enhancements in SAM on fuel axial expansion reactivity feedback modeling for stationary liquid fuel and on decay heat modeling for stationary fuel. Section 4 discusses the development of control and trip systems in SAM. Section 5 describes additional fluid and solid property models implemented in SAM as built-in materials, including salt, lead, lead-bismuth, and a number of fuel and cladding materials. The code validation efforts are summarized in Section 6.

### **1.1 Overview of Current Capabilities**

For a system analysis code, numerical methods, mesh management, equations of state, fluid properties, solid material properties, neutronics properties, pressure loss and heat transfer closure laws, and good user input/output interfaces are all indispensable. SAM leverages the MOOSE framework and its dependent libraries to provide solver schemes, mesh management, and I/O interfaces while focusing on new physics and component model development for advanced reactor

systems. The developed physics and component models provide the following major modeling features:

1. One-D pipe networks represent general fluid systems such as the reactor coolant loops.
2. Flexible integration of fluid and solid components, able to model complex and generic engineering systems. A general liquid flow and solid structure interface model was developed for easier implementation of physics models in the components. Flexible multi-scale convective heat transfer modeling is available through coupled 1D fluid flow and 2D/3D heat structure or coupled 2D/3D flow with 2D/3D heat structure.
3. A pseudo three-dimensional capability by physically coupling the 1-D or 2-D components in a 3-D layout. For example, the 3-D full-core heat-transfer in an SFR reactor core can be modeled. The heat generated in the fuel rod of one fuel assembly can be transferred to the coolant in the core channel, the duct wall, the inter-assembly gap, and then the adjacent fuel assemblies.
4. Pool-type reactor specific features such as liquid volume level tracking, cover gas dynamics, heat transfer between 0-D pools, fluid heat conduction, etc. These are important features for accurate safety analyses of SFRs or other advanced reactor concepts.
5. A computationally efficient multi-dimensional flow model, for thermal mixing and stratification phenomena in large enclosures for safety analysis. It was noted that an advanced and efficient multi-D flow modeling capability embedded in a system analysis code is very desirable to improve the accuracy of advanced reactor safety analyses and to reduce modeling uncertainties.
6. A general mass transport capability has been implemented in SAM based on the passive scalar transport. The code can track any number of species carried by the fluid flow for various applications.
7. A general control and trip system modeling capability. A set of PID controllers and Boolean logic units are available.
8. A general fluid freezing and thawing capability. This capability is particularly important for safety assessments of molten-salt-cooled reactors.
9. An infrastructure for coupling with external codes has been developed and demonstrated. The code coupling with STAR-CCM+, SAS4A/SASSYS-1, Mammoth/RattleSnake, Nek5000, and BISON have been demonstrated.

As an example, SAM simulation results of a heat-pipe-cooled micro reactor are shown in Figure 1-1 and Figure 1-2. This effort utilized several MOOSE-based submodules under NRC's Comprehensive Reactor Analysis Bundle (CRAB), including SAM, MAMMOTH/Rattlesnake, and MOOSE's Tensor Mechanics module. The details of this work are summarized in an earlier report [13].

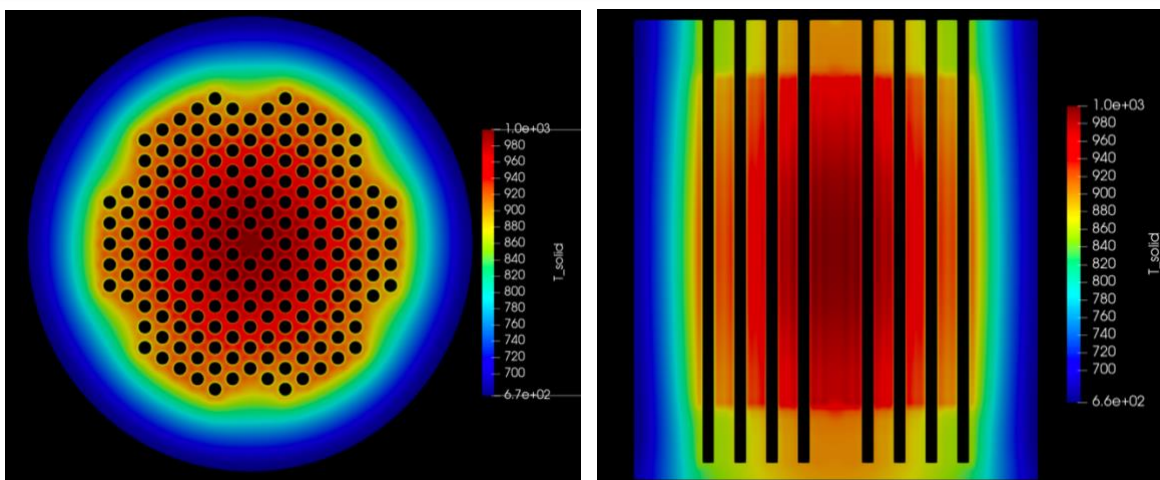


Figure 1-1. Steady state solid temperature profile of a heat-pipe-cooled micro reactor. Horizontal cut view (left) and vertical cut view (right).

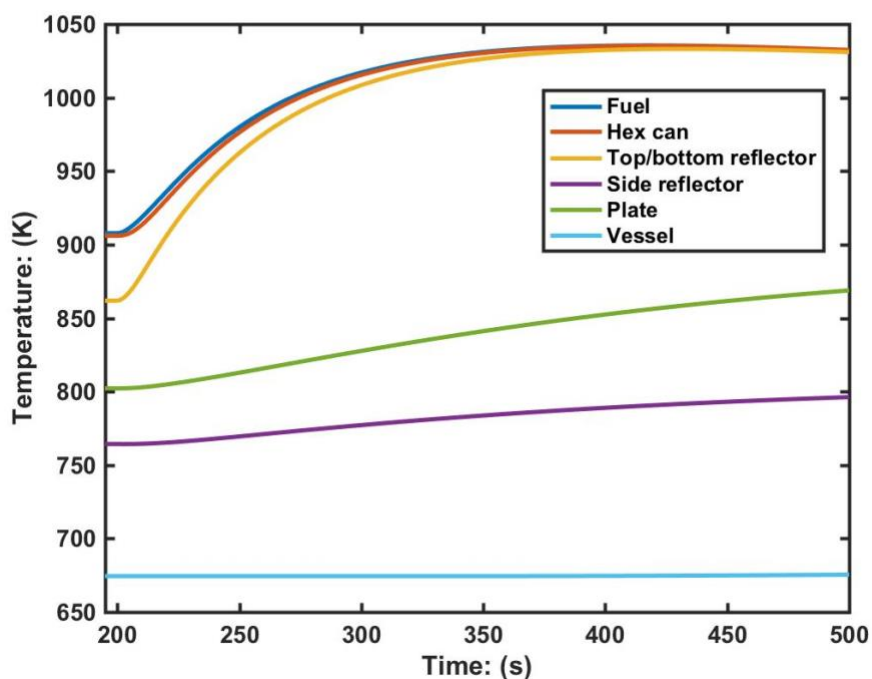


Figure 1-2. Transient average solid temperature of different blocks during an unprotected loss of heat sink event.

## 2 Updates in Multi-Dimensional Flow Modeling

In SAM, a unified multi-dimensional flow model has been developed and implemented to consider both the general multi-dimensional flow model and the porous medium-based flow model, as both models have many similarities. Additionally, there is also a need to include both flow models in the same simulations for many applications. For example, in simulations of HTGR core multi-dimensional flows, it is typical to model flows in both the top and bottom plena using the general multi-dimensional flow model and flow through the pebble-bed core using the porous-medium approach. Therefore, a unified model based on these two sets of flow equations has been developed to reduce the effort of code implementation, as well as to ease the model input process when both flow models are needed in the same simulation. The details of this work are summarized in an earlier report [7], including the governing equations, types of boundary conditions, stabilization schemes, and code implementation of the SAM multi-dimensional model.

For the unified flow model, the fluid mass, momentum, and energy balance equations are given as follows:

$$\epsilon \frac{\partial \rho}{\partial t} + \nabla \cdot (\rho \mathbf{v}) = 0, \quad (2-1)$$

$$\rho \frac{\partial \mathbf{v}}{\partial t} + \frac{\rho}{\epsilon} (\mathbf{v} \cdot \nabla) \mathbf{v} + \epsilon \nabla p - \epsilon \rho \mathbf{g} + \mathbf{F}_m = 0, \quad (2-2)$$

$$\epsilon \rho c_p \frac{\partial T}{\partial t} + \rho c_p \mathbf{v} \cdot \nabla T - \nabla \cdot (\epsilon k \nabla T) - q''' + S_e = 0 \quad (2-3)$$

The source term,  $\mathbf{F}_m$ , in the momentum equation is given as

$$\mathbf{F}_m = \begin{cases} -\mu \nabla^2 \mathbf{v} & (\text{general model}) \\ \alpha \mathbf{v} + \beta |\mathbf{v}| \mathbf{v} & (\text{porous - medium model}) \end{cases} \quad (2-4)$$

and the additional source term in the energy equation,  $S_e$ , in the fluid energy equation is given as

$$S_e = \begin{cases} 0 & (\text{general model}) \\ a_w h(T - T_s) & (\text{porous - medium model}) \end{cases} \quad (2-5)$$

It is noted that, if the porosity  $\epsilon = 1$ , this model exactly reduces to the general multi-dimensional flow model. For the simulation of a porous medium, where the solid structure is also modeled, an additional solid-phase energy equation is used.

$$(1 - \epsilon) \rho_s c_{p,s} \frac{\partial T_s}{\partial t} - \nabla \cdot (k_{s,eff} \nabla T_s) - q_s''' + a_w h(T_s - T) = 0. \quad (2-6)$$

To validate SAM's multi-dimensional flow model for more complex flows with turbulence mixing and thermal-stratification phenomena, experimental data obtained in the SUPERCARVNA facility are utilized. The SUPERCARVNA facility at the French Alternative Energies and Atomic Energy Commission (CEA) was designed to study liquid sodium flows relevant to SFRs, including flow recirculation and thermal stratification. This facility consists of a stainless-steel rectangular cavity with inlet and outlet channels at the bottom of the cavity. The cavity's right wall can be

heated through a secondary sodium loop (heating channel), while all the other walls are thermally insulated. The facility and flow directions are illustrated in Figure 2-1.

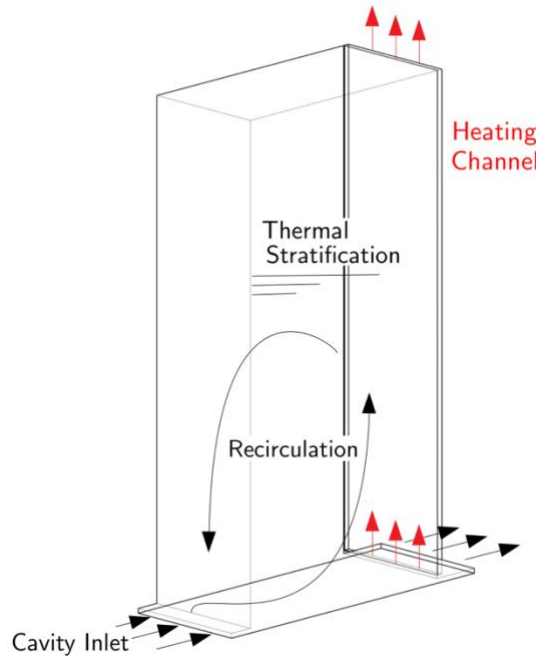


Figure 2-1. The SUPERCARVNA facility and flow directions.

Three experimental data sets were utilized to validate SAM's multi-dimensional flow model: one transient case and two steady-state cases. The steady-state cases consist of flows with a strong buoyancy presence induced by the heating channel. The transient case, on the other hand, consists of a forced-convection experiment, where liquid sodium is injected at a constant flow rate with decreasing temperatures. Although the geometry of the SUPERCARVNA facility is quite simple, the flow conditions are indeed complex, and pose great challenges for numerical simulations because of the very different length scales in the test facility. The SAM code validation study started with the use of the highly simplified zero-equation turbulence model, and it was determined that this model is too simple to capture the complex flow and thermal mixing behaviors. Subsequently, the code validation continued with the use of turbulent viscosity data from high-resolution STAR-CCM+ CFD simulations to improve the accuracy of the results. Using this approach, the SAM simulation results showed very good agreement with both the SUPERCARVNA experimental data and STAR-CCM+ simulation results, as shown in Figure 2-2 and Figure 2-3. The details of this work are summarized in an earlier report [7].

This work presents an attempt to include a built-in advanced multi-dimensional flow model in SAM to overcome the simulation challenges of thermal mixing and stratification. This new code capability has been successfully validated against the very complex SUPERCARVNA transient and steady-state experimental data. This result shows that the SAM code has a very high potential to effectively treat the thermal mixing and stratification phenomena that pose significant challenges to traditional system analysis codes.



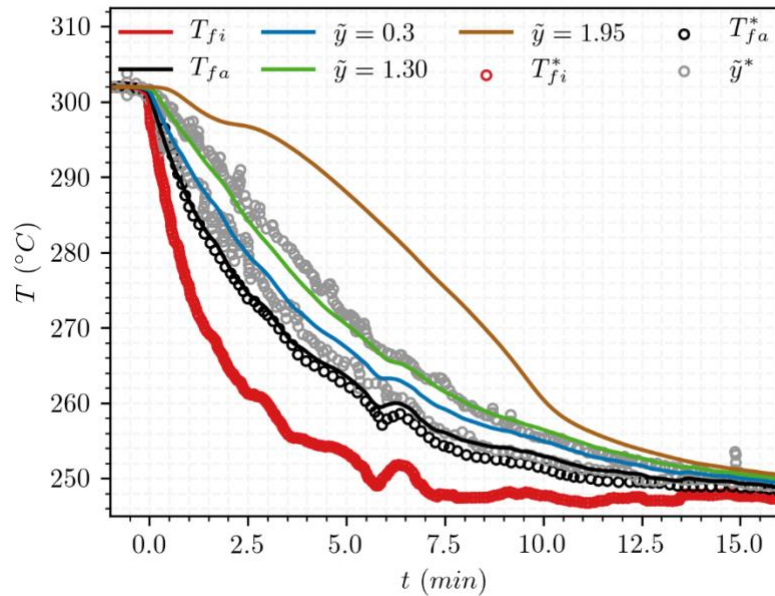


Figure 2-2. SAM results for case T1: Temperature time series at the inlet  $T_{fi}$ , outlet  $T_{fa}$ , and several  $\tilde{y}$  locations (along V2). The circles and solid lines represent the experimental data and the SAM results, respectively. Note that  $T_{fi}$  is overlapping with  $T_{fi}^*$ .

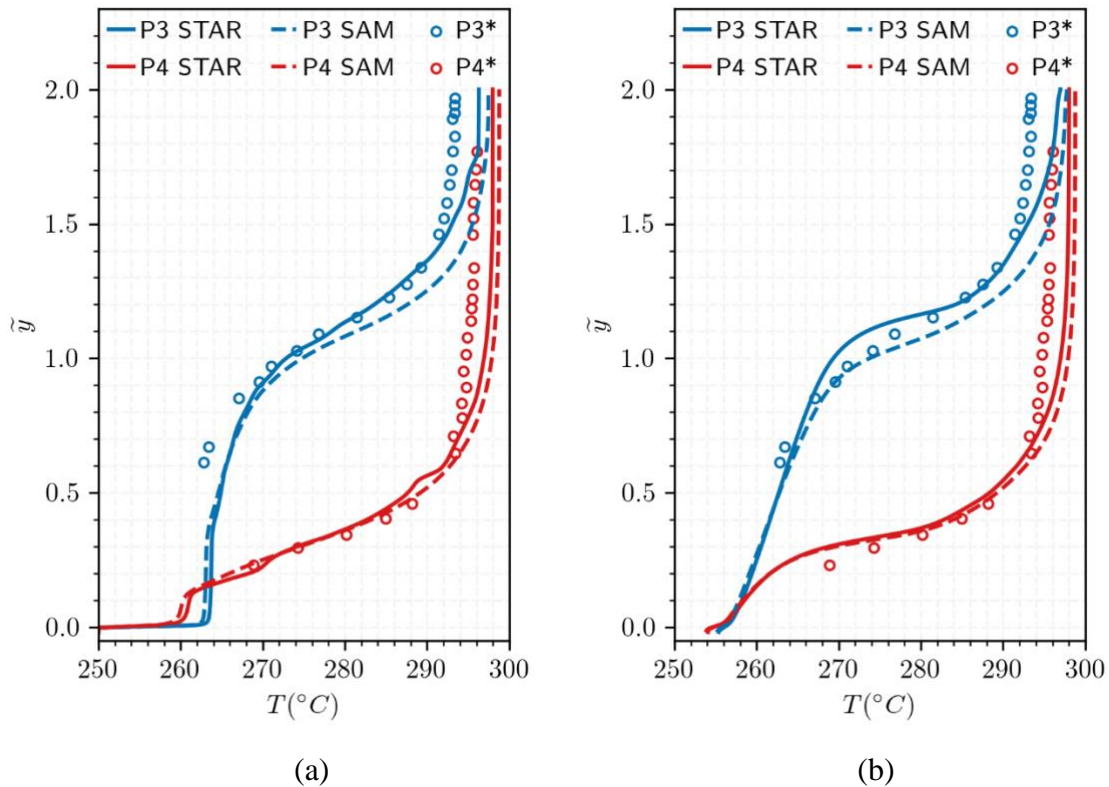


Figure 2-3. CFD, SAM, and experimental temperature profiles for cases P3 and P4 at locations a) V1 and b) V2. The circles and solid lines represent the experimental data and the CFD results, respectively. The dashed lines represent the SAM results.

### 3 SAM Enhancements in Reactivity Feedback and Decay Heat Modeling

The analysis of the transient behavior of a nuclear reactor requires the coupled simulation of reactor kinetics and thermal hydraulics of the reactor core, especially for those unprotected transients where the reactor scram system may not function properly. The point-kinetics model has been widely used for reactor safety analysis due to its simplicity to capture the transient behavior. Various reactivity feedback models have been developed and integrated with the point-kinetics module, including fuel axial expansion, core radial expansion, fuel Doppler, and coolant density reactivity. The reactivity feedback models in SAM are similar to the respective models used in SAS4A/SASSYS-1. The point-kinetics module and reactivity feedback models were summarized in an earlier report [14].

#### 3.1 Fuel Axial Expansion Reactivity Feedback

In the point-kinetics model, it is assumed that the reactor power can be separated into space and time functions. The assumption is adequate when the space distribution remains nearly constant during the transient. The point-kinetics model shown in Equations (3-1) and (3-2) has been widely used for the transient safety analysis of stationary fuel reactors.

$$\frac{dn}{dt} = \frac{\rho_{ext} - \tilde{\beta}_{eff}}{\Lambda} n(t) + \sum_i \lambda_i C_i \quad (3-1)$$

$$\frac{dC_i}{dt} = \frac{\beta_i}{\Lambda} n(t) - \lambda_i C_i \quad (3-2)$$

where  $n(t)$  is the total neutron population, normalized by the neutron population at full fission power;  $C_i$  is the magnitude of delayed-neutron precursor population  $i$ , normalized by the neutron population at full fission power;  $\tilde{\beta}_{eff}$  is the total effective delayed-neutron fraction while  $\beta_i$  is the fraction for delayed neutron precursor  $i$ ;  $\rho_{ext}$  is representing the net reactivity feedback;  $\Lambda$  is the prompt neutron generation time. The normalized fission power and delayed-neutron precursor population are solved simultaneously.

In advanced nuclear reactors (e.g. sodium-cooled fast reactor), the fuel, especially metallic fuel, expands or shrinks within the cladding in response to the fuel temperature changes during the transient. The geometry changes of the fuel impose a positive or negative reactivity feedback, which affects the prompt fission power calculation in the point-kinetics model. The fuel axial expansion model was developed to consider the reactivity feedback in response to the fuel temperature changes during the transient. In SAM, the fuel axial expansion reactivity is calculated by the difference between the transient and initial values of total reactivity worth in the fuel pins.

$$R_A(t) = \int_{z=0}^{z=L'} \rho_f(\xi, t) \times f(\xi) \times A d\xi \quad (3-3)$$

$$\Delta R_A(t) = R_A(t) - R_A^{ss} \quad (3-4)$$

where  $\Delta R_A$  is the fuel axial expansion reactivity feedback in the unit of  $\Delta k/k$ ;  $\rho_f(\xi, t)$  is the fuel density at transient time  $t$  in the unit of  $kg/m^3$ ;  $f(\xi)$  is the fuel reactivity coefficient in unit of



$\Delta k/k$  / kg;  $L'$  and  $A$  are the expanded fuel length during the transient and cross-section area, respectively. The integration will consider the axial thermal expansion of the fuel pin.

Considering dividing the fuel into  $N$  number of layers in the axial direction, the integral reactivity worth was calculated by

$$R_A(t) = \sum_{i=1}^N m_i f(\xi_i) \quad (3-5)$$

where  $m_i$  is the mass of the  $i$ -th axial layer which is held constant during the transient calculation due to mass conservation,  $\xi_i$  is the axial center location of the  $i$ -th layer with the axial displacement in consideration.

This model and the implementation worked well for the solid fuel where the axial expansion is small. However, this model faces some issues in case of liquid fuel design, such as the Stable Salt Reactor (SSR) design by Moltex Energy:

- The assumption of linear thermal expansion was valid for solid fuel where the thermal expansion is relatively small. However, this assumption becomes problematic in the case of a liquid fuel, as used in molten-salt reactors, where the axial thermal expansion (and fuel density change) could be significant. The fuel density changes nonlinearly with fuel temperature.
- During the transient, there could be a portion of fuel outside the nominal fuel length due to the thermal expansion. The exact reactivity worth of this portion of fuel needs to be provided by the reactor physics calculation. In the SAM implementation, the value of fuel reactivity function ( $f$ ) beyond the nominal fuel length represents this effect. This is understood as an input that should be provided by the SAM users. In practice, this information could be difficult to obtain. In the case of solid fuel, because the thermal expansion is small, the effect of this portion of fuel is minimal and can be safely ignored. However, this is not the case for liquid fuel.

To overcome these issues, a new fuel axial expansion reactivity feedback model is added into SAM for better treatment of liquid fuel. In this new model, the density change of the fuel during the transient is directly used in estimating the reactivity. Let the mesh size be  $\Delta z$ . Let  $f_i$  and  $\rho_i$  be the reactivity worth and fuel density at the  $i$ -th layer. The fuel axial expansion reactivity inside the fixed mesh (i.e. the nominal fuel length region) is evaluated with

$$\Delta R' = \sum_{i=1}^N [\rho_i(t) - \rho_i^{ss}] f_i A \Delta z \quad (3-6)$$

where  $\rho_i$  is temperature dependent during the transient. The reactivity contribution of the fuel beyond the fixed mesh is considered by

$$\Delta R^* = f^* \rho_N(t) A [L' - L] \quad (3-7)$$

where  $f^*$  is the value of fuel reactivity function beyond the fixed mesh,  $\rho_N(t)$  is the density of the last layer of fuel, and  $L'$  is the expanded fuel length during the transient.  $L'$  is calculated from the fuel density change using mass conservation. The total fuel axial expansion reactivity is

$$\Delta R_A(t) = \Delta R' + \Delta R^* = \sum_{i=1}^N [\rho_i(t) - \rho_i^{ss}] f_i A \Delta z + f^* \rho_N(t) A [L'(t) - L]. \quad (3-8)$$

This new model avoids the assumption of linear thermal expansion by using directly the fuel density change with fuel temperature and is thus valid for liquid fuel. Additionally, the new model considers the reactivity contribution from the fuel expanded outside the nominal fuel length.

Numerical tests are performed to compare the existing model (for solid fuel) and the new model (for liquid fuel). The test cases are designed with the following conditions:

- At the steady state, the fuel has a uniform temperature of  $T_0 = 273.15$  K.
- At the transient time, the fuel density is  $\rho_0 = 1458.3$  kg/m<sup>3</sup>.
- At the transient time, the fuel has a temperature increase of  $\Delta T = 20$  K.
- The fuel linear thermal expansion coefficient is  $\alpha = 1.76 \times 10^{-5}$  K<sup>-1</sup>.
- The fuel area is  $A = 3.14159 \times 10^{-2}$  m<sup>2</sup>.
- The fuel length is  $L_0 = 0.8$  m.
- A total of  $N = 20$  layers are used in the uniform mesh. The mesh size is  $\Delta z = 0.04$  m.

Four separate tests are performed using different reactivity worth functions, shown in Figure 3-1.

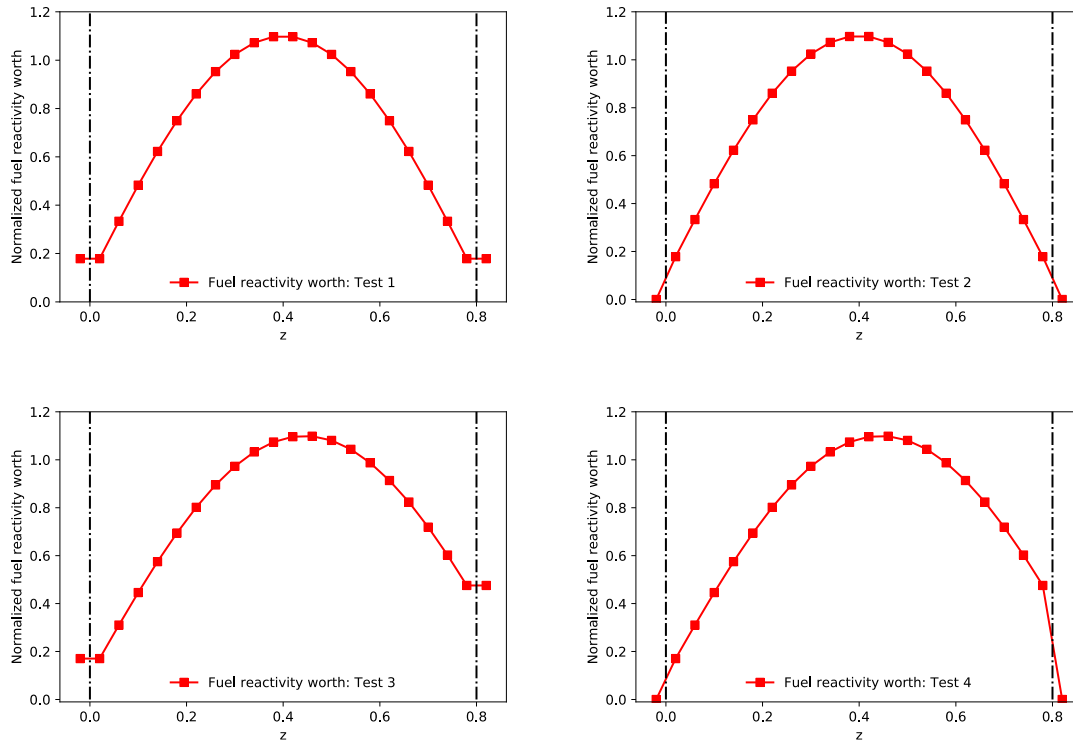


Figure 3-1. Normalized fuel reactivity worth profile at different axial layers for the numerical tests.

The test results are listed in Table 3-1. The thermal expansion in these tests are not significant, but the difference between the two models is observed. In practical simulations where the liquid fuel thermal expansion is significant, the new liquid fuel model is expected to treat the fuel axial expansion reactivity feedback more accurately.

Table 3-1: Comparison of SAM fuel axial expansion reactivity feedback models for solid fuel and liquid fuel.

Test No.	Liquid fuel model	Solid fuel model	Relative Difference
Test 1	-7.207 E-05	-7.209 E-05	3.52 E-04
Test 2	-9.508 E-05	-9.454 E-05	-5.70 E-03
Test 3	-4.065 E-05	-4.165 E-05	2.45 E-02
Test 4	-1.020 E-04	-1.014 E-04	-5.04 E-03

### 3.2 Decay Heat Implementation in SAM

The decay heat model of the ANS standard, ANSI/ANS-5.1-2005 [15], was implemented in SAM firstly for flowing fuel applications (MSR) [16]. The ANS standard has four decay curves corresponding to U-235, U-238, Pu-239, and Pu-241 fission. The SAM decay heat model was extended for stationary fuel applications, utilizing the same ANS standard. All labels used in the equations implemented in SAM for the solid fuel decay heat calculation are listed in Table 3-2.

Table 3-2: Description of notations used in equations.

Term	Unit	Meaning
$f_j(t)$	MeV/fission-s	Decay power $t$ seconds after a fission event from isotope $j$ .
$\alpha_{i,j}$	MeV/fission-s	Tabulated data from ANS standard.
$\lambda_{i,j}$	s <sup>-1</sup>	Tabulated data from ANS standard.
$P_d(t)$	W	Decay heat power
$P_f(t)$	W	Prompt fission power
$Q_f$	MeV/fission	Prompt recoverable energy per fission
$C_1$	J/MeV	$C_1 = 1.602 \times 10^{-13}$
$F(t)$	Fission/s	Total fission rate $F(t) = \frac{P_f(t)}{Q_f C_1}$
$H_{i,j}(t)$	J	Amount of fictitious decay heat precursor
$\beta_{i,j}$		$\beta_{i,j} = \frac{\alpha_{i,j}}{\lambda_{i,j} Q_f}$
$j$		Index $j$ refers to the four isotopes (U-235, U-238, Pu-239, Pu-241).

In ANS standards, the decay heat power at time  $t$  for a fission event from isotope  $j$  occurring at time 0 is express as:

$$f_j(t) = \sum_i \alpha_{i,j} e^{-\lambda_{i,j} t}. \quad (3-9)$$

In which  $\alpha_{i,j}$  and  $\lambda_{i,j}$  are tabulated data from ANS standards. Then, the decay power can be expressed as:

$$P_d(t) = \sum_j \int_{-\infty}^t \frac{P_f(t')}{Q_f C_1} C_1 f_j(t - t') dt', \quad (3-10)$$

with  $t$  and  $t'$  defined in Figure 3-2.

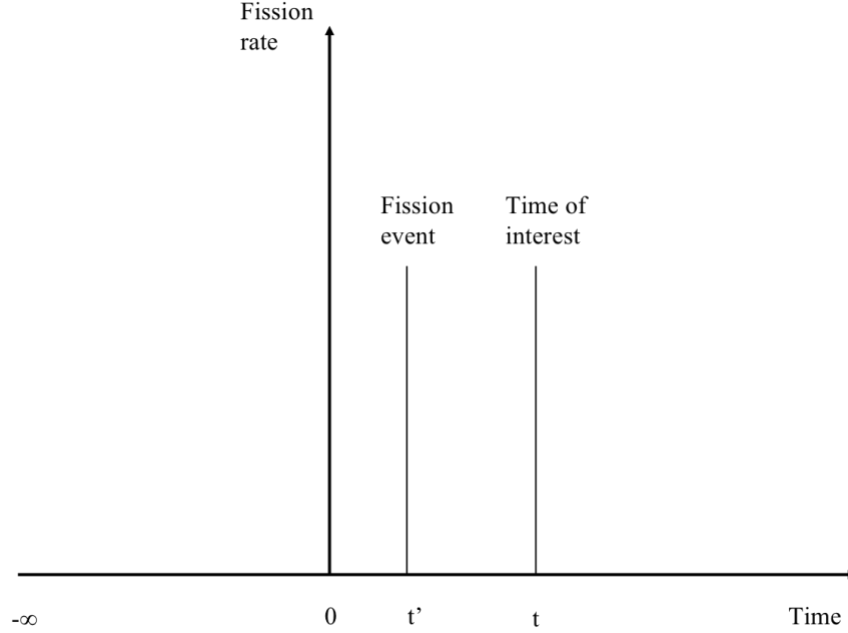


Figure 3-2. Detailed time notation for decay heat modeling.

The amount of decay heat precursor  $H_{i,j}(t)$  is defined as

$$H_{i,j}(t) = \int_{-\infty}^t F(t') C_1 \left( \frac{\alpha_{i,j}}{\lambda_{i,j}} \right) e^{-\lambda_{i,j}(t-t')} dt' \quad (3-11)$$

So that

$$P_d(t) = \sum_j \sum_i \lambda_{i,j} H_{i,j}(t) \quad (3-12)$$

For initial condition of decay heat precursors:

$$H_{i,j}(t=0) = \int_{-\infty}^0 P_f(t') \beta_{i,j} e^{\lambda_{i,j} t'} dt'. \quad (3-13)$$

In the current implementation,  $P_f(t')$  is assumed to be constant before  $t = 0$ , so

$$H_{i,j}(0) = \frac{P_f(-\infty) \beta_{i,j}}{\lambda_{i,j}}, \quad (3-14)$$

$$P_d(0) = \sum_j \sum_i P_f(-\infty) \beta_{i,j}. \quad (3-15)$$

At a given time step  $t_k$ , we would have:

$$H_{i,j}(t_k + \Delta t) = \int_{-\infty}^{t_k + \Delta t} P_f(t') \beta_{i,j} e^{-\lambda_{i,j}(t_k + \Delta t - t')} dt' \quad (3-16)$$

$$H_{i,j}(t_k + \Delta t) = \int_{-\infty}^{t_k} P_f(t') \beta_{i,j} e^{-\lambda_{i,j}(t_k + \Delta t - t')} dt' + \int_{t_k}^{t_k + \Delta t} P_f(t') \beta_{i,j} e^{-\lambda_{i,j}(t - t')} dt' \quad (3-17)$$

$$H_{i,j}(t_k + \Delta t) = H_{i,j}(t_k) e^{-\lambda_{i,j} \Delta t} + \int_{t_k}^{t_k + \Delta t} P_f(t') \beta_{i,j} e^{-\lambda_{i,j}(t - t')} dt' \quad (3-18)$$

It is further assumed that  $P_f(t')$  is a 2<sup>nd</sup>-order polynomial function of  $t'$  within  $\Delta t$ . The coefficients of the polynomial can be solved by polynomial fitting using the data from the two earlier time steps. Then, the integral can be analytically integrated.

There are four tests developed to verify the decay heat implementation. A summary of the tests is given in Table 3-3. Test 3 is more complicated in the sense that the fission power is not a constant function over time. The fission power is solved by the point kinetic equation implemented in SAM, thus we selected special values for the parameters used in the point kinetic equation so that the fission power solution is a combination of exponential functions. In this case, the left hand of Eq. (3-11) can be analytically integrated.

Table 3-3: Decay heat verification tests result summary.

Test #	0	1	2	3
Operating power (W)	0	1.0E6	1.0E6	100.0
$P_f(t > 0)$ (W)	100 <sup>1</sup>	0 <sup>2</sup>	0 <sup>2</sup>	Vary with time
Fission fraction	100% U-235	100% U-235	100% Pu-239	100% U-235
Analytical solution	$H_i(t) = \frac{100\beta_i}{\lambda_i} (1 - e^{-\lambda_i t})$	$H_i(t) = H_i(0) e^{-\lambda_i t}$	$H_i(t) = H_i(0) e^{-\lambda_i t}$	- <sup>3</sup>
Maximum relative error	1.83x10 <sup>-7</sup>	8.88x10 <sup>-15</sup>	9.52x10 <sup>-10</sup>	- <sup>3</sup>

1. By setting the external reactivity of the point kinetic equation to zero.
2. Point kinetic equation was not evoked.
3. Test 3 is elaborated in the paragraphs following the table.

For the point kinetic equations Eq. (3-1) and (3-2), we chose  $\rho$  to be 0.1,  $\beta$  to be 0.1,  $\Lambda$  to be 1/60, and  $\lambda$  to be 1.0 (the subscript is dropped to indicate we only used 1 precursor group for this test case). Then, the point kinetic equations can be simplified as:

$$\frac{dn}{dt} = C \text{ and } \frac{dC}{dt} = 6n - C.$$

The two ODEs can be easily solved and yield the solution:

$$n(t) = Ae^{-3t} + Be^{2t},$$

where the constant  $A$  and  $B$  can be obtained from the initial condition ( $n(0) = 100.0$ ,  $C(0) = 0.0$ ). The analytical solution for the decay heat is compared with the SAM solution in Figure 3-3. The difference between the solutions are presented in Figure 3-4. It was observed that the difference is  $\sim 10\%$  at the initial time step and drops down quickly after a few time steps. This is caused by the representation of decay heat as a post-processor. The decay heat post processor is calculated at the beginning of each time step. As a result of this, it does not have the information regarding to the fission power at the current time step. The difference is the most significant for decay heat at the initial time step. As the decay heat builds up, the difference becomes negligible since the decay is a cumulative quantity that depends on the time from the start to the current time step, i.e., the difference from the initial time step is smeared out.

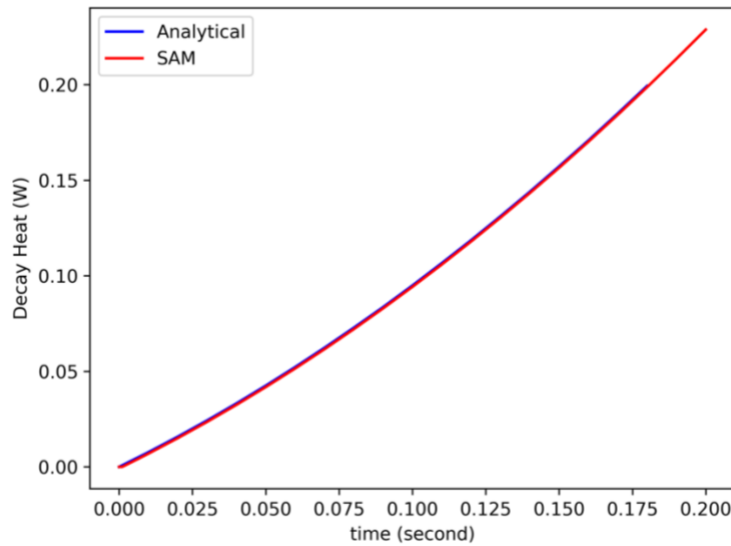


Figure 3-3. Test 3 decay heat from analytical and SAM solutions.

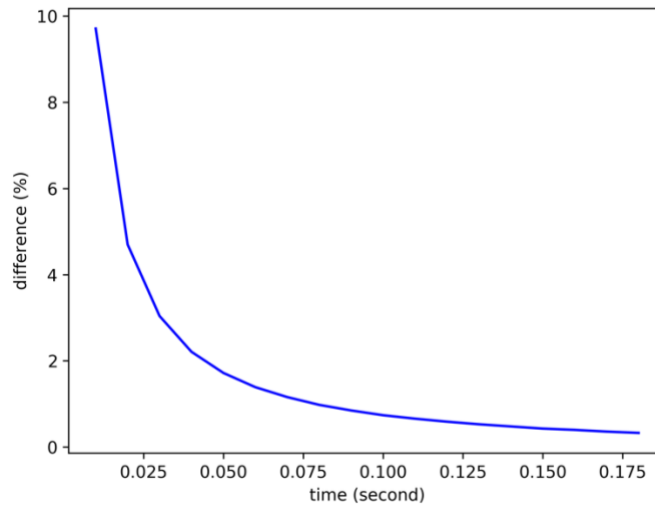


Figure 3-4. Relative difference between the analytical and SAM solutions for Test 3.

## 4 Control and Trip System Modeling

The capability to simulate the industrial control and trip systems is essential to a modern nuclear system analysis software, as the control and trip systems play a fundamental role in the nuclear power plant. The SAM control and trip systems are aimed to provide the capability to simulate the control and trip systems typically used in hydrodynamic systems. The control system is used to perform the evaluation of algebraic and simple ordinary differential equations (e.g. integration and differentiation); while the trip system is used to perform the evaluation of logical statements.

### 4.1 General design feature

The control and trip systems are developed based on the *GeneralUserObject* of MOOSE. The hierarchy of classes of control and trip systems model is shown in Figure 4-1, where the control and trip components are implemented as *ControlSystem* and *TripSystem* classes, respectively. They are derived from a common parent class *CTGeneric* which handles generic functions of the two type of components including the interface obtaining input signals, execution steps, and input processing.

There are several classes further derived from *ControlSystem* such as *CSAddition*, *CSDivision*, and others, each representing a control component performing a specific operation. Table 4-1 lists the operations that the control components perform, where  $Y$  represents output,  $V$  represents inputs, and other parameters represents constants. Similarly, there are three classes *TSBoolean*, *TSComparison*, and *TSDelay* derived from *TripSystem*, representing the trip components performing Boolean operations, comparison, and delay respectively. Table 4-2 lists the operations that the trip components perform, where  $T_r$  represents trip signal,  $V$  represents input control signal, and  $OP$  represents operation. For the trip components, *TSBoolean* and *TSComparison* are implemented to allow latched or unlatched trip signal. For a latched component, the output is set only at the first time when the trip condition is met, and it does not reset the trip component if the condition is not met later. For unlatched component, it sets or resets the output whenever the condition is met or isn't met.

Users can build a control or trip system diagram flexibly by connecting the components. To connect two control and trip components, the input to the downstream component must be the name of the upstream component, and the type of the input must be *ControlSystem* or *TripSystem*. When the value of the downstream component is evaluated, it will first try to obtain the values of the upstream components. The evaluation process propagates from the downstream to the upstream until the entire diagram is evaluated. In fact, the control and trip models also allow users to specify types of inputs other than *ControlSystem* and *TripSystem*, such as function, constant, scalar variables, or postprocessor. However, these types are supposed to be used for the inputs of components which are not connected to any upstream control or trip components but are provided by either users or other SAM models.

Control and trip system models are implemented as *GeneralUserObject*, which are executed only once at the end of the time step. Such an implementation decouples the models from the rest of SAM iterations, i.e., the outputs of control and trip systems depend on the users inputs or variables of other SAM models such as pressures and temperatures at the previous time step, but they do not change during the iterations of the current time step. The coupled system, depending on the transfer functions of the system and designs of the control and trip, can be unstable. The

implementation is intended to avoid non-convergence associated with the potential instability when both control and trip variables and those of other SAM models are changing at the same time. It is also computationally inexpensive because the models are executed only once per time step.

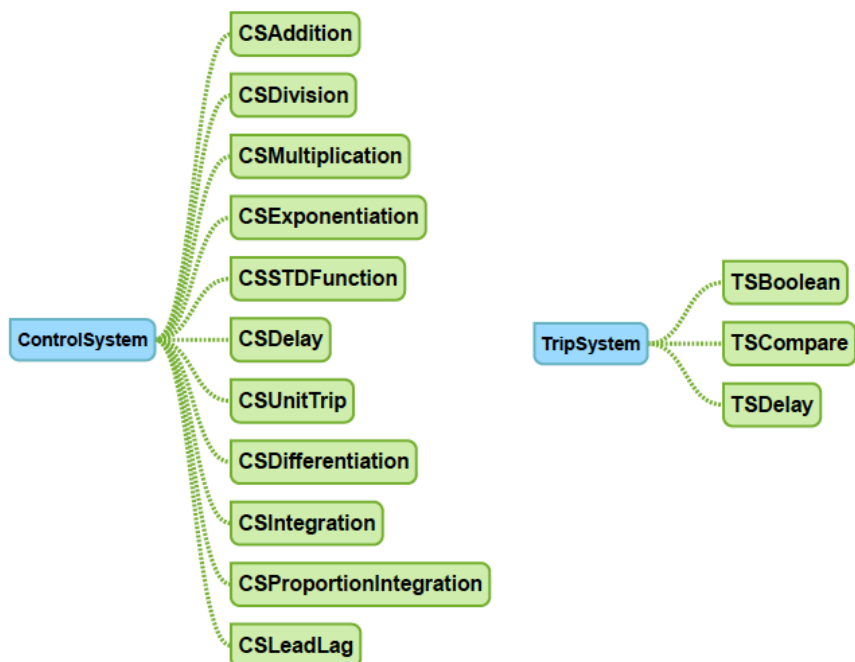


Figure 4-1. Hierarchy of classes for control and trip system models.



Table 4-1: Operations of control components

t	Name	Operation
1	CSAddition	$Y = S(A_0 + \sum_{i=1}^N A_i V_i)$
2	CSDelay	$Y = S V_1(t - t_d)$ , where t is time, and $t_d$ is the delay time
3	CSDifferentiation	$Y = S dV_1/dt$
4	CSDivision	$Y = \frac{S}{V_1}$ , or $S \frac{V_2}{V_1}$
5	CSExponentiation	$Y = S V_1^x$ , or $S V_1^{V_2}$ , where x is a constant exponent
6	CSIntegration	$Y = S \int_{t_0}^t V_1 dt$
7	CSLeadLag	$Y + A_2 \frac{dY}{dt} = S(V_1 + \frac{A_1 dV_1}{dt})$ with $A_2 Y(0) = S A_1 V_1(0)$
8	CSMultiplication	$Y = S \prod_{i=1}^N V_i$
9	CSProportion-Integration	$Y = S(A_1 V_1 + A_2 \int_{t_0}^t V_1 dt)$
10	CSSTDFunction	$Y = S F(V_1, V_2, \dots)$ where F is mathematic function including $\sin(V_1)$ , $\cos(V_1)$ , $\tan(V_1)$ , $\sinh(V_1)$ , $\cosh(V_1)$ , $\tanh(V_1)$ , $ V_1 $ , $\ln(V_1)$ , $\exp(V_1)$ , $\sqrt{V_1}$ , $\min(V_1, V_2, \dots)$ , and $\max(V_1, V_2, \dots)$
11	CSUnitTrip	$Y = S U(\pm t_r)$ , where $t_r$ is a trip signal. The “-” sign represents complement of the signal. U takes value of 0 if the trip signal is false, and 1 if the trip signal is true

Table 4-2: Operations of trip components.

Index	Name	Operation
1	TSCompare	$T_r = V_1 \text{ OP } (V_2 + C)$ , where OP is one of the operations of EQ (equal), NE (not equal), GT (greater than), GE (greater than or equal), LT (less than) and LE (less than or equal).
2	TSBoolean	$T_r = T_{r,1} \text{ OP } T_{r,2}$ , where OP is one of the Boolean operations of AND, OR, NAND (not-and), NOR (not-or), XOR (exclusive or), XNOR (exclusive NOR), and NOT (complement). For NOT, the second input is not required.
3	TSDelay	$T_r = T_{r,1}(t - t_d)$ , where t is time and $t_d$ is the delay time

## 4.2 Testing

A number of verification tests are developed for the control and trip system models. The purposes of the these tests are to ensure the control and trip component models are correctly implemented, and the performances of the models are reasonable. A few of those tests are briefly discussed here.

### 4.2.1 Case 1: Component test

An ad-hoc example control/trip system is created to verify control/trip system design. The purpose of this test is to examine whether the functions of the control and trip components are correctly implemented. Figure 4-2 shows the diagram of the test which includes 11 components covering the majority of control and trip components currently implemented. Table 4-3 lists the parameters, inputs and expected outputs of each components. SAM results of final outputs  $y_1$  and  $y_2$  and each components are compared with the expected values in Figure 4-3 and Figure 4-4, and

they match each other closely. This indicates that the component models are correctly implemented.

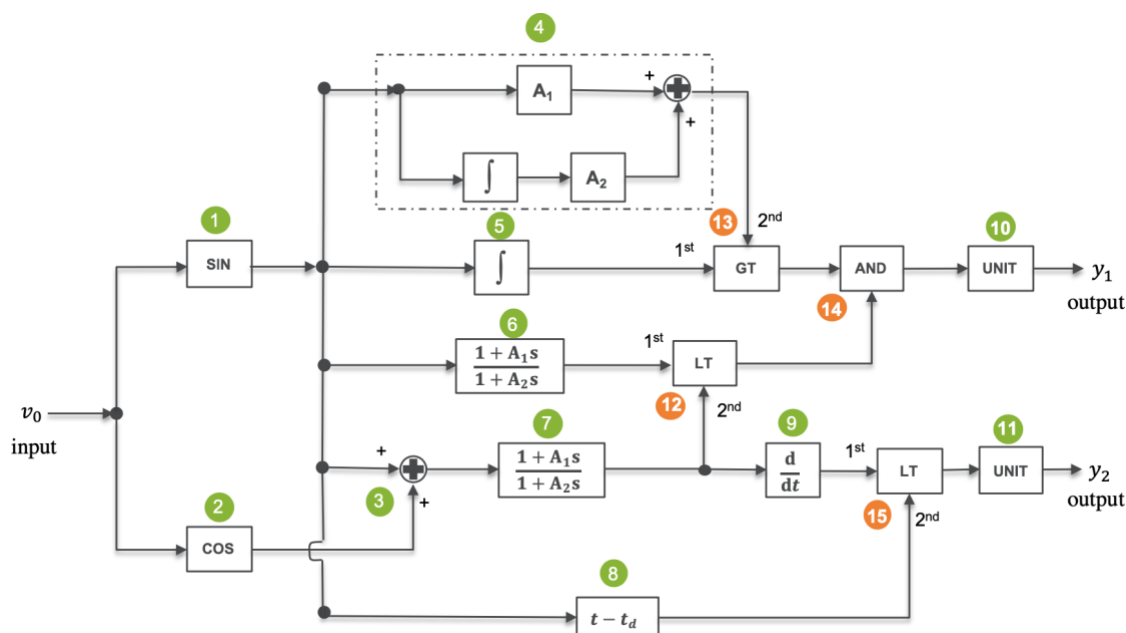


Figure 4-2. Diagram for test case 1: component test.

Table 4-3: Components in the test case 1.

ID	Type	Parameters	Input	Expected output
1	CSSTDFunction	SIN	$t$	$\sin(t)$
2	CSSTDFunction	COS	$t$	$\cos(t)$
3	CSAddition	$A_1 = 1, A_2 = 1$	$\sin(t), \cos(t)$	$\sin(t) + \cos(t)$
4	CSProportionIntegration	$A_1 = 1, A_2 = 1$	$\sin(t)$	$1 - \cos(t) + \sin(t)$
5	CSIntegration	—	$\sin(t)$	$1 - \cos(t)$
6	CSLeadLag	$A_1 = 1, A_2 = 0$	$\sin(t)$	$\sin(t) + \cos(t)$
7	CSLeadLag	$A_1 = 0, A_2 = 1$	$\sin(t) + \cos(t)$	$\sin(t)$
8	CSDelay	$t_d = \pi/2$	$\sin(t)$	$\sin(\max(t - t_d, 0))$
9	CSDifferentiation	—	$\sin(t)$	$\cos(t)$
10	CSUnitTrip	—	—	—
11	CSUnitTrip	—	—	—
12	TSCmpare	LT	—	—
13	TSCmpare	GT	—	—
14	TSBoolean	AND	—	—
15	TSCmpare	LT	—	—

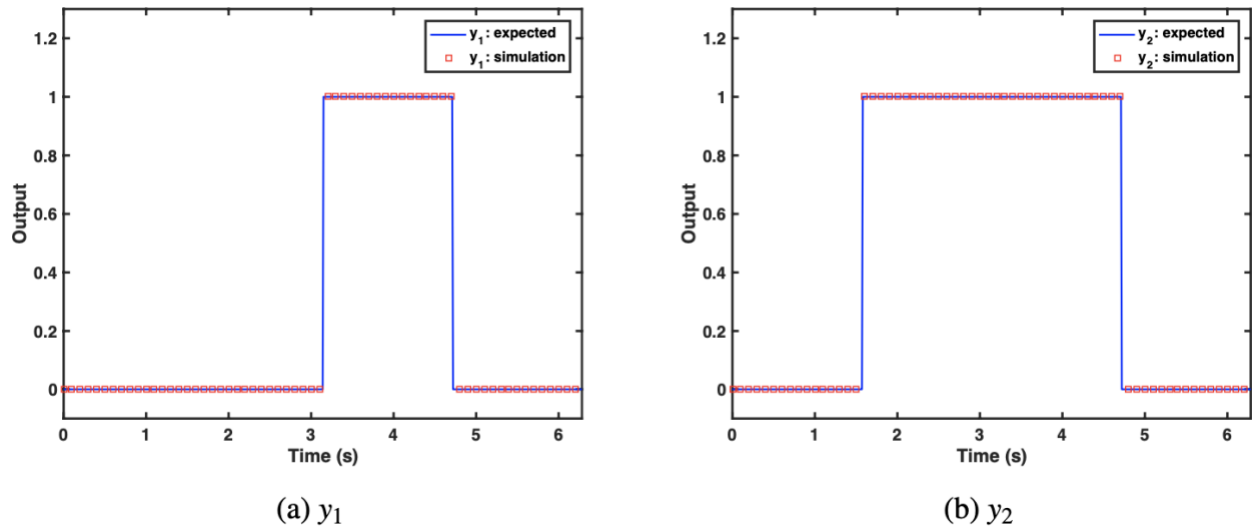


Figure 4-3. Comparisons of outputs  $y_1$  and  $y_2$  for case 1: component test.

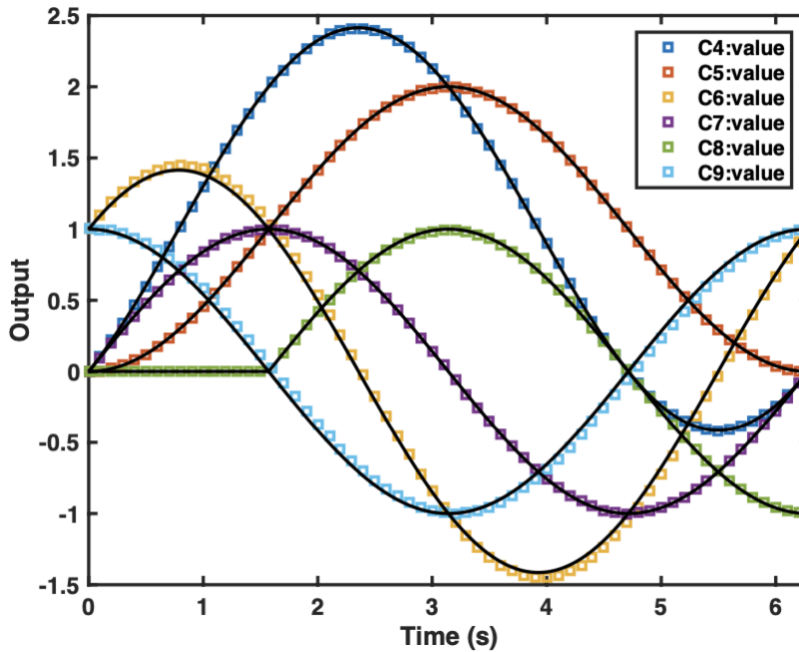


Figure 4-4. Comparisons of values of each component for case 1: component test.

#### 4.2.2 Case 2: Mass flow controller

The purpose of this test is to demonstrate the capabilities and performances of control and trip models through an example of mass flow rate controller. In this test, a core channel is modeled with a cylindrical fuel pin and liquid metal coolant. Constant 30 kW of power is generated in the fuel and transferred to the coolant. The temperature at the inlet of the core channel is held constant, but the inlet velocity is varying. Figure 4-5 shows the diagram for this test, which includes one proportional-integration controller for the inlet velocity. The input of the controller is the difference between the outlet temperature of the core channel and a user-specified outlet temperature. The output of the controller is added to a constant velocity specified by users to

control the inlet velocity of the core channel. In this example, if the temperature is different between the outlet temperature and the specified outlet temperature, the controller will increase or decrease the inlet velocity accordingly so that the outlet temperature follows the specified outlet temperature. Figure 4-6 shows the observed outlet temperature follows the specified outlet temperature reasonably well. The code runs smoothly without evident slowing down due to non-convergence or instability.

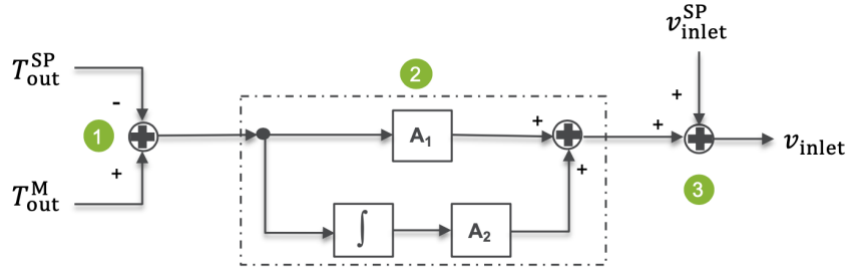


Figure 4-5. Diagram for test case 2: mass flow controller.

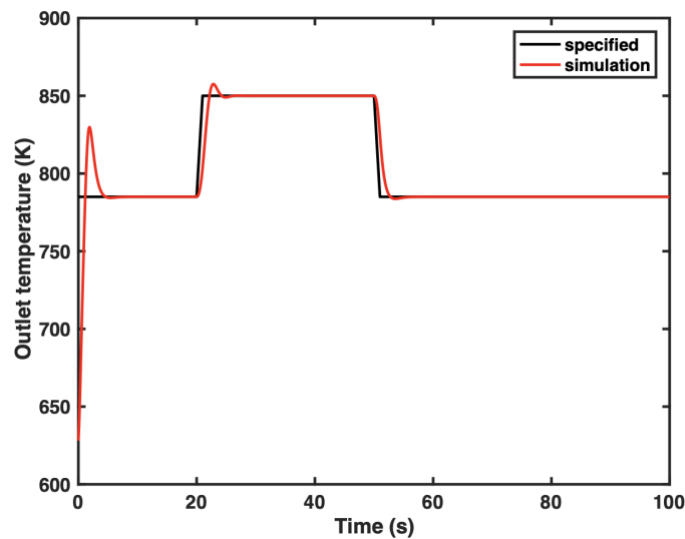


Figure 4-6. Comparison of outlet temperature and specified temperature for test case 2: mass flow controller.

#### 4.2.3 Case 3: Reactivity controller

The purpose of this test is to demonstrate the capabilities and performances of control and trip models through an example of reactivity controller. In this test, a core channel is simulated with point kinetics model. A control system is built to control the reactor power in the core channel through external reactivity imposed to the point kinetics model. Figure 4-7 shows the control diagram for this test, which has one proportional-integration controller. The input of the controller is the difference between the reactor power and a user-specified power. The output of the controller is subtracted by the total reactivity feedback and imposed as the external reactivity to control the power. In this test, if the power is different from the specified power, a net reactivity will be inserted or extracted from the core accordingly, and the point kinetics model drives the power to

follow the specified power. Figure 4-8 shows that the reactor power follows the specified power reasonably well. The code runs smoothly without evident slowing down due to non-convergence or instability.

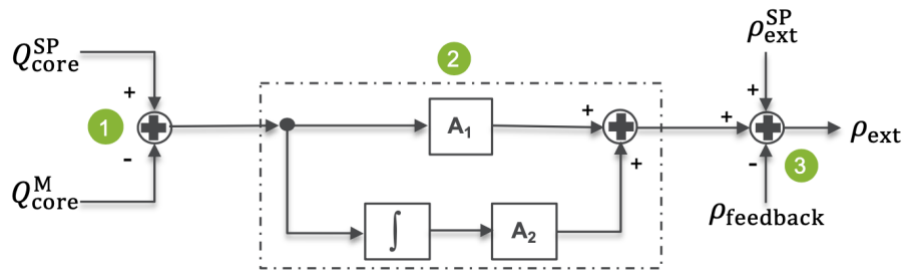


Figure 4-7. Diagram for test case 3: reactivity controller.

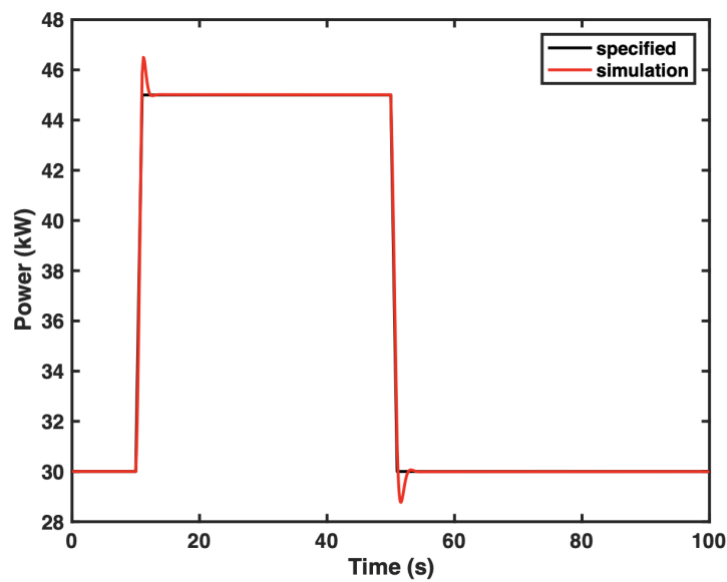


Figure 4-8. Comparison of reactor fission power and specified power for test case 3: reactivity controller.

## 5 Fluid and Solid Property Model Updates

The material property models are required to close the governing fluid flow and heat conduction equations. The dependency of fluid properties and their partial derivatives on the state variables (pressure and temperature) are implemented in the SAM Equation of State (EOS) model. A number of fluid properties, such as sodium, air, salts like FLiBe and FLiNaK, have been implemented in SAM. Leveraging the molten salt reactor thermophysical properties database that is under development in DOE-NE's Advanced Reactor Technology Molten Salt Reactor Campaign, additional molten salt property models have been implemented in SAM in FY20. Additionally, lead, lead-bismuth eutectic alloy, and several commonly used fuel and cladding material properties were recently implemented in SAM.

### 5.1 Salt Properties and Equation-of-State

#### 5.1.1 Pure Salt Property Modeling

In the Molten Salt Thermophysical Properties Database [17] under development, temperature dependent correlations for density, viscosity, thermal conductivity, and heat capacity are presented. These correlations are proposed for 27 different pure salts. Out of these 27 salts, 10 of these correlations were complete enough to be included in SAM. The 10 salts and their thermophysical correlations are shown below:

LiF (temperature in K):

$$\begin{aligned}\rho &= 1000 \cdot (2.4 - 0.00049 \cdot T) \quad \left(\frac{\text{kg}}{\text{m}^3}\right) \\ \mu &= 0.001 \cdot (0.18 \cdot e^{\frac{22000}{8.3145 \cdot T}}) \quad \left(\frac{\text{kg}}{\text{m} \cdot \text{s}}\right) \\ c_p &= 2467.289 \quad \left(\frac{\text{J}}{\text{kg} \cdot \text{K}}\right) \\ k &= 1.4 \quad \left(\frac{\text{W}}{\text{m} \cdot \text{K}}\right)\end{aligned}\tag{5-1}$$

NaF (temperature in K):

$$\begin{aligned}\rho &= 1000 \cdot (2.8 - 0.00064 \cdot T) \quad \left(\frac{\text{kg}}{\text{m}^3}\right) \\ \mu &= 0.001 \cdot (0.12 \cdot e^{\frac{26000}{8.3145 \cdot T}}) \quad \left(\frac{\text{kg}}{\text{m} \cdot \text{s}}\right) \\ c_p &= 1667.13 \quad \left(\frac{\text{J}}{\text{kg} \cdot \text{K}}\right) \\ k &= 0.9 \quad \left(\frac{\text{W}}{\text{m} \cdot \text{K}}\right)\end{aligned}\tag{5-2}$$

KF (temperature in K):

$$\begin{aligned}\rho &= 1000 \cdot (2.6 - 0.00065 \cdot T) \quad \left(\frac{\text{kg}}{\text{m}^3}\right) \\ \mu &= 0.001 \cdot (0.11 \cdot e^{\frac{24000}{8.3145 \cdot T}}) \quad \left(\frac{\text{kg}}{\text{m} \cdot \text{s}}\right) \\ c_p &= 1239.313 \quad \left(\frac{\text{J}}{\text{kg} \cdot \text{K}}\right) \\ k &= 0.57 \quad \left(\frac{\text{W}}{\text{m} \cdot \text{K}}\right)\end{aligned}\tag{5-3}$$

BeF<sub>2</sub> (temperature in K):

$$\begin{aligned}\rho &= 1000 \cdot (2.0 - 0.000015 \cdot T) \quad \left(\frac{\text{kg}}{\text{m}^3}\right) \\ \mu &= 0.001 \cdot (3 \cdot 10^{-7} \cdot e^{\frac{240000}{8.3145 \cdot T}}) \quad \left(\frac{\text{kg}}{\text{m} \cdot \text{s}}\right) \\ c_p &= (10 - 0.0015 \cdot T - 1.6 \cdot 10^7 \cdot T^{-2} + 3.0 \cdot 10^{-9} \cdot T^2) / (0.047) \quad \left(\frac{\text{J}}{\text{kg} \cdot \text{K}}\right) \\ k &= 0.8 \quad \left(\frac{\text{W}}{\text{m} \cdot \text{K}}\right)\end{aligned} \tag{5-4}$$

LiCl (temperature in K):

$$\begin{aligned}\rho &= 1000 \cdot (1.9 - 0.00043 \cdot T) \quad \left(\frac{\text{kg}}{\text{m}^3}\right) \\ \mu &= 0.001 \cdot (0.11 \cdot e^{\frac{19000}{8.3145 \cdot T}}) \quad \left(\frac{\text{kg}}{\text{m} \cdot \text{s}}\right) \\ c_p &= 1486.059 \quad \left(\frac{\text{J}}{\text{kg} \cdot \text{K}}\right) \\ k &= 0.73 \quad \left(\frac{\text{W}}{\text{m} \cdot \text{K}}\right)\end{aligned} \tag{5-5}$$

NaCl (temperature in K):

$$\begin{aligned}\rho &= 1000 \cdot (2.1 - 0.00054 \cdot T) \quad \left(\frac{\text{kg}}{\text{m}^3}\right) \\ \mu &= 0.001 \cdot (0.089 \cdot e^{\frac{22000}{8.3145 \cdot T}}) \quad \left(\frac{\text{kg}}{\text{m} \cdot \text{s}}\right) \\ c_p &= 1163.530 \quad \left(\frac{\text{J}}{\text{kg} \cdot \text{K}}\right) \\ k &= 0.49 \quad \left(\frac{\text{W}}{\text{m} \cdot \text{K}}\right)\end{aligned} \tag{5-6}$$

KCl (temperature in K):

$$\begin{aligned}\rho &= 1000 \cdot (2.4 - 0.00049 \cdot T) \quad \left(\frac{\text{kg}}{\text{m}^3}\right) \\ \mu &= 0.001 \cdot (0.062 \cdot e^{\frac{25000}{8.3145 \cdot T}}) \quad \left(\frac{\text{kg}}{\text{m} \cdot \text{s}}\right) \\ c_p &= 992.605 \quad \left(\frac{\text{J}}{\text{kg} \cdot \text{K}}\right) \\ k &= 0.74 \quad \left(\frac{\text{W}}{\text{m} \cdot \text{K}}\right)\end{aligned} \tag{5-7}$$

MgCl<sub>2</sub> (temperature in K):

$$\begin{aligned}\rho &= 1000 \cdot (2.0 - 0.00027 \cdot T) \quad \left(\frac{\text{kg}}{\text{m}^3}\right) \\ \mu &= 0.001 \cdot (0.18 \cdot e^{\frac{21000}{8.3145 \cdot T}}) \quad \left(\frac{\text{kg}}{\text{m} \cdot \text{s}}\right) \\ c_p &= (92 - 2 \cdot 10^{-6} \cdot T + 5.9 \cdot 10^6 \cdot T^{-2}) / (0.095211) \quad \left(\frac{\text{J}}{\text{kg} \cdot \text{K}}\right) \\ k &= 0.2 \quad \left(\frac{\text{W}}{\text{m} \cdot \text{K}}\right)\end{aligned} \tag{5-8}$$

CaCl<sub>2</sub> (temperature in K):

$$\begin{aligned}\rho &= 1000 \cdot (2.5 - 0.00042 \cdot T) \quad \left(\frac{\text{kg}}{\text{m}^3}\right) \\ \mu &= 0.001 \cdot (0.1 \cdot e^{\frac{30000}{8.3145 \cdot T}}) \quad \left(\frac{\text{kg}}{\text{m} \cdot \text{s}}\right) \\ c_p &= 901.031 \quad \left(\frac{\text{J}}{\text{kg} \cdot \text{K}}\right) \\ k &= 0.45 \quad \left(\frac{\text{W}}{\text{m} \cdot \text{K}}\right)\end{aligned} \tag{5-9}$$

SrCl<sub>2</sub> (temperature in K):

$$\begin{aligned}\rho &= 1000 \cdot (3.4 - 0.00058 \cdot T) \quad \left(\frac{\text{kg}}{\text{m}^3}\right) \\ \mu &= 0.001 \cdot (0.096 \cdot e^{\frac{35000}{8.3145 \cdot T}}) \quad \left(\frac{\text{kg}}{\text{m} \cdot \text{s}}\right) \\ c_p &= 630.811 \quad \left(\frac{\text{J}}{\text{kg} \cdot \text{K}}\right) \\ k &= 0.38 \quad \left(\frac{\text{W}}{\text{m} \cdot \text{K}}\right)\end{aligned} \tag{5-10}$$

### 5.1.2 Mixed Salt Property Modeling

In the Molten Salt Thermophysical Properties Database, there are temperature dependent correlations for density, viscosity, thermal conductivity, and heat capacity for different salt mixtures. Correlations are set up for 36 different mixed salts, although almost all of them are incomplete. Future work will be needed to have more complete correlations. Of the mixed salts, it was determined that one (LiF-NaF-KF) was complete enough to be included in SAM. For this mixed salt, the density correlation has an uncertainty of 2%, the viscosity correlation has an uncertainty of 2%, the heat capacity correlation has an uncertainty of 10%, and the thermal conductivity correlation has an uncertainty of 5%. Note the LiF-NaF-KF correlations in the database are slightly different from those of FLiNaK that was previously implemented in SAM. Both set of models are available in SAM now.



LiF-NaF-KF (temperature in K):

*Composition (Mole %):* 0.465 – 0.115 – 0.42

$$\begin{aligned}
 \rho &= 1000 \cdot (2.6 - 0.00062 \cdot T) \left( \frac{\text{kg}}{\text{m}^3} \right), & 940 < T < 1170 \\
 \mu &= 0.001 \cdot \left( 0.025 \cdot e^{\frac{4500}{8.3145 \cdot T}} \right) \left( \frac{\text{kg}}{\text{m}} \cdot \text{s} \right), & 770 < T < 970 \\
 c_p &= (980 + 1.1 \cdot T) / (0.126) \left( \frac{\text{J}}{\text{kg} \cdot \text{K}} \right) \\
 k &= 0.36 - 0.00056 \cdot T \left( \frac{\text{W}}{\text{m} \cdot \text{K}} \right), & 790 < T < 1080
 \end{aligned} \tag{5-11}$$

### 5.1.3 MSRE Fuel Property Modeling

Fission product data for numerous and varied samples taken during the Molten Salt Reactor Experiment (MSRE) was compiled and reported in an MSRE report [18]. This includes physical properties of the MSRE fuel salt used in the experiment. The temperature dependent models of the MSRE fuel salt that were reported are implemented into SAM. The MSRE fuel salt contains LiF, BeF<sub>2</sub>, ZrF<sub>4</sub>, UF<sub>4</sub>, Cr, Fe, Ni. For this MSRE fuel, the temperature correlations that are currently implemented in SAM are shown below:

$$\begin{aligned}
 \rho &= 1000 \cdot (2.575 - 0.000513 \cdot (T - 273.15)) \left( \frac{\text{kg}}{\text{m}^3} \right), & \pm 1\% \text{ Precision} \\
 \mu &= 0.001 \cdot \left( 0.116 \cdot e^{\frac{3755}{T}} \right) \left( \frac{\text{kg}}{\text{m}} \cdot \text{s} \right), & \pm 7\% \text{ Precision} \\
 c_p &= 2386.47 \left( \frac{\text{J}}{\text{kg} \cdot \text{K}} \right), & \pm 3\% \text{ Precision} \\
 k &= 0.01 \left( \frac{\text{W}}{\text{m} \cdot \text{K}} \right), & \pm 10\% \text{ Precision}
 \end{aligned} \tag{5-12}$$

## 5.2 Liquid Metal Property Modeling

The Handbook on Lead-bismuth Eutectic Alloy and Lead Properties, Materials Compatibility, Thermal-hydraulics and Technologies [19] contains comprehensive temperature dependent property models on density, viscosity, heat capacity, thermal conductivity, and enthalpy. The recommended temperature dependent correlations of lead, bismuth, and LBE are implemented in SAM. The relative precision and uncertainty vary depending on which other available models these correlations are compared to. For density, the deviation of the lead model does not exceed 2%, the deviation of the bismuth model does not exceed 1.3%, and the deviation of lead-bismuth eutectic does not exceed 0.8%. For viscosity, the estimated uncertainty of the lead model is 5%, the deviation of the bismuth model does not exceed 5%, and the deviation of lead-bismuth eutectic does not exceed 8%. For heat capacity, the maximum deviation from accepted models is 10%, the deviation of the bismuth model does not exceed 2%, and the deviation of lead-bismuth eutectic does not exceed 5%. For thermal conductivity, the estimated uncertainty is 15% for lead, 15%, for bismuth, and the deviation of lead-bismuth eutectic from accepted models does not exceed 15%. The correlations implemented in SAM are shown below:

Lead (temperature in K):

$$\begin{aligned}\rho &= 11441 - 1.2795 \cdot T \left( \frac{\text{kg}}{\text{m}^3} \right) \\ \mu &= 4.55 \cdot 10^{-4} \cdot e^{\frac{1069}{T}} \left( \frac{\text{kg}}{\text{m}} \cdot \text{s} \right), \quad 600.6 < T < 1473 \\ c_p &= 176.2 - 4.923 \cdot 10^{-2} \cdot T + 1.544 \cdot 10^{-5} \cdot T^2 - 1.524 \cdot 10^6 \cdot T^{-2} \left( \frac{\text{J}}{\text{kg} \cdot \text{K}} \right), \quad 600.6 < T < 2021 \\ k &= 9.2 + 0.011 \cdot T \left( \frac{\text{W}}{\text{m} \cdot \text{K}} \right), \quad 600.6 < T < 1300 \\ \Delta h &= 176.2 \cdot (T - T_m) - 2.4616 \cdot 10^{-2} \cdot (T^2 - T_m^2) + 5.147 \cdot 10^{-6} \cdot (T^3 - T_m^3) + 1.524 \cdot 10^6 \\ &\quad \cdot (T^{-1} - T_m^{-1}) \left( \frac{\text{J}}{\text{kg}} \right)\end{aligned}$$

Bismuth (temperature in K):

$$\begin{aligned}\rho &= 10725 - 1.22 \cdot T \left( \frac{\text{kg}}{\text{m}^3} \right) \\ \mu &= 4.456 \cdot 10^{-4} \cdot e^{\frac{780}{T}} \left( \frac{\text{kg}}{\text{m}} \cdot \text{s} \right), \quad 544.6 < T < 1300 \\ c_p &= 118.2 + 5.934 \cdot 10^{-3} \cdot T + 7.183 \cdot 10^6 \cdot T^{-2} \left( \frac{\text{J}}{\text{kg} \cdot \text{K}} \right), \quad 544.6 < T < 1831 \\ k &= 7.34 + 9.5 \cdot 10^{-3} \cdot T \left( \frac{\text{W}}{\text{m} \cdot \text{K}} \right), \quad 544.6 < T < 1000 \\ \Delta h &= 118.2 \cdot (T - T_m) - 2.967 \cdot 10^{-3} \cdot (T^2 - T_m^2) - 7.183 \cdot 10^6 \cdot (T^{-1} - T_m^{-1}) \left( \frac{\text{J}}{\text{kg}} \right)\end{aligned}$$

Lead-Bismuth Eutectic (temperature in K):

$$\begin{aligned}\rho &= 11065 - 1.293 \cdot T \left( \frac{\text{kg}}{\text{m}^3} \right) \\ \mu &= 4.94 \cdot 10^{-4} \cdot e^{\frac{754.1}{T}} \left( \frac{\text{kg}}{\text{m}} \cdot \text{s} \right), \quad 400 < T < 1173 \\ c_p &= 164.8 - 3.94 \cdot 10^{-2} \cdot T + 1.25 \cdot 10^{-5} \cdot T^2 - 4.56 \cdot 10^5 \cdot T^{-2} \left( \frac{\text{J}}{\text{kg} \cdot \text{K}} \right), \quad 400 < T < 1100 \\ k &= 3.284 + 1.617 \cdot 10^{-2} \cdot T - 2.305 \cdot 10^{-6} \cdot T^2 \left( \frac{\text{W}}{\text{m} \cdot \text{K}} \right) \\ \Delta h &= 164.8 \cdot (T - T_m) - 1.97 \cdot 10^{-2} \cdot (T^2 - T_m^2) + 4.167 \cdot 10^{-6} \cdot (T^3 - T_m^3) + 4.56 \cdot 10^5 \\ &\quad \cdot (T^{-1} - T_m^{-1}) \left( \frac{\text{J}}{\text{kg}} \right)\end{aligned}$$

### 5.3 Solid Properties

SAM provides users with the option to manually input temperature-dependent solid property models that can be used in simulation. This user option is maintained, but a material library containing correlations for solid properties was implemented. This library will be expanded in the future to provide improved user experience.

#### 5.3.1 Clad Property Modeling

Currently, two different types of stainless steels, HT9 and D9, are implemented in SAM. Correlations for specific heat, thermal expansion, density and thermal conductivity were taken from references [20], [21], and [22]. These correlations are shown below.

HT9 (temperature in K):

$$c_p = \frac{1}{6}(T - 227) + 500 \left( \frac{\text{J}}{\text{kg} \cdot \text{K}} \right), \quad T < 527 \text{ } ^\circ\text{C}$$

$$c_p = \frac{3}{5}(T - 527) + 550 \left( \frac{\text{J}}{\text{kg} \cdot \text{K}} \right), \quad T > 527 \text{ } ^\circ\text{C}$$

$$\alpha = \frac{-0.2191 + 5.678 \cdot 10^{-4} \cdot T + 8.111 \cdot 10^{-7} \cdot T^2 - 2.576 \cdot 10^{-10} \cdot T^3}{100} (\text{K}^{-1})$$

$$\rho = \frac{7800}{1 + 3\alpha} \left( \frac{\text{kg}}{\text{m}^3} \right)$$

$$k = 17.622 + 2.428 \cdot 10^{-2} \cdot T - 1.696 \cdot 10^{-5} \cdot T^2 \left( \frac{\text{W}}{\text{m} \cdot \text{K}} \right), \quad 500 \text{ K} < T < 1030 \text{ K}$$

$$k = 12.027 + 1.218 \cdot 10^{-2} \cdot T \left( \frac{\text{W}}{\text{m} \cdot \text{K}} \right), \quad 1030 \text{ K} < T < 1200 \text{ K}$$

D9 (temperature in K):

$$c_p = 431 + 17.7 \cdot 10^{-2} \cdot T + 8.72 \cdot 10^{-5} / T^2 \left( \frac{\text{J}}{\text{kg} \cdot \text{K}} \right),$$

$$\alpha = \frac{-0.4247 + 1.282 \cdot 10^{-3} \cdot T + 7.362 \cdot 10^{-7} \cdot T^2 - 2.069 \cdot 10^{-10} \cdot T^3}{100} (\text{K}^{-1})$$

$$\rho = \frac{7800}{1 + 3\alpha} \left( \frac{\text{kg}}{\text{m}^3} \right)$$

$$k = 7.598 + 2.391 \cdot 10^{-2} \cdot T - 8.899 \cdot 10^{-6} \cdot T^2 \left( \frac{\text{W}}{\text{m} \cdot \text{K}} \right), \quad 500 \text{ K} < T < 1030 \text{ K}$$

$$k = 7.260 + 1.509 \cdot 10^{-2} \cdot T \left( \frac{\text{W}}{\text{m} \cdot \text{K}} \right), \quad 1030 \text{ K} < T < 1200 \text{ K}$$

### 5.3.2 Fuel Property Modeling

Thermal physical properties of a few fuel types, i.e. UO<sub>2</sub>, MOX, U-Pu-Zr, are also implemented in SAM for user friendliness. The irradiated thermal conductivity for UO<sub>2</sub> and MOX are also provided. The correlations taken from references [23]-[29] were combined to allow for complete density, thermal conductivity, and heat capacity correlations. In the table below, the coefficients used for the heat capacity calculations of UO<sub>2</sub> and MOX are provided.

Table 5-1: Constants Used in Heat Capacity Correlations for UO<sub>2</sub> and MOX.

Constant	UO <sub>2</sub>	MOX	Units
C <sub>1</sub>	302.27	322.49	J/kg/K
C <sub>2</sub>	8.463 · 10 <sup>-3</sup>	1.4679 · 10 <sup>-2</sup>	J/kg/K <sup>2</sup>
C <sub>3</sub>	8.741 · 10 <sup>7</sup>	0	J/kg
θ	548.68	587.41	K
E <sub>a</sub>	18531.7	0	K

UO2 (temperature in K):

$$\rho_f = \frac{10970}{1 + 2.04 \cdot 10^{-5}(T - 273) + 8.79 \cdot 10^{-2}(T - 273)^2} \left( \frac{\text{kg}}{\text{m}^3} \right), \quad T < T_{\text{solidus}}$$

$$\rho_f = \frac{\rho_{f\text{-solidus}}}{1 + 0.07338 \frac{T - T_{\text{sol}}}{T_{\text{liq}} - T_{\text{sol}}}} \left( \frac{\text{kg}}{\text{m}^3} \right), \quad T_{\text{liquidus}} < T < T_{\text{solidus}}$$

$$\rho_f = \frac{\rho_{f\text{-liquidus}}}{1 + \frac{0.9285(T - T_{\text{liq}})}{8860 - 0.9285(T - T_{\text{liq}})}} \left( \frac{\text{kg}}{\text{m}^3} \right), \quad T > T_{\text{liquidus}}$$

$$c_p = C_1(\theta/T)^2 \cdot \frac{\exp\left(\frac{\theta}{T}\right)}{\left[\exp\left(\frac{\theta}{T}\right) - 1\right]^2} + 2C_2T + C_3E_a \exp(-E_a/T)T^2 \left( \frac{\text{J}}{\text{kg} \cdot \text{K}} \right)$$

$$k_0 = (0.06059 + 0.2754 \sqrt{2 - \frac{O}{M} + 2.011 \cdot 10^{-4} \cdot T})^{-1} + \frac{4.715 \cdot 10^9}{T^2} \exp\left(\frac{-16361}{T}\right) + 0.2 \left( \frac{\text{W}}{\text{m} \cdot \text{K}} \right)$$

MOX (temperature in K):

$$\rho_f = \frac{11460}{1 + 2.04 \cdot 10^{-5}(T - 273) + 8.79 \cdot 10^{-2}(T - 273)^2} \left( \frac{\text{kg}}{\text{m}^3} \right), \quad T < T_{\text{solidus}}$$

$$\rho_f = \frac{\rho_{f\text{-solidus}}}{1 + 0.07338 \frac{T - T_{\text{sol}}}{T_{\text{liq}} - T_{\text{sol}}}} \left( \frac{\text{kg}}{\text{m}^3} \right), \quad T_{\text{liquidus}} < T < T_{\text{solidus}}$$

$$\rho_f = \frac{\rho_{f\text{-liquidus}}}{1 + \frac{0.9285(T - T_{\text{liq}})}{8860 - 0.9285(T - T_{\text{liq}})}} \left( \frac{\text{kg}}{\text{m}^3} \right), \quad T > T_{\text{liquidus}}$$

$$c_p = C_1(\theta/T)^2 \cdot \frac{\exp\left(\frac{\theta}{T}\right)}{\left[\exp\left(\frac{\theta}{T}\right) - 1\right]^2} + 2C_2T + C_3E_a \exp(-E_a/T)T^2 \left( \frac{\text{J}}{\text{kg} \cdot \text{K}} \right)$$

$$k_0 = (0.06059 + 0.2754 \sqrt{2 - \frac{O}{M} + 2.011 \cdot 10^{-4} \cdot T})^{-1} + \frac{4.715 \cdot 10^9}{T^2} \exp\left(\frac{-16361}{T}\right) \left( \frac{\text{W}}{\text{m} \cdot \text{K}} \right)$$

U-Pu-Zr (temperature in K):

$$\rho = \left( \frac{W_{\text{Zr}}}{6500} + \frac{W_{\text{UPu}}}{19000} \right)^{-1} \cdot (1 - P - 0.015 \cdot Bu) / (1 + 6 \cdot 10^{-5}(T - 293.15)) \left( \frac{\text{kg}}{\text{m}^3} \right)$$

$$c_{p1} = 26.58 + \frac{0.027}{\text{Molar Mass}} T \left( \frac{\text{J}}{\text{kg} \cdot \text{K}} \right), \quad T < 868.15 \text{ K} = T_1$$

$$c_{p2} = 15.84 + \frac{0.026}{\text{Molar Mass}} T \left( \frac{\text{J}}{\text{kg} \cdot \text{K}} \right), \quad 868.15 \text{ K} < T < 923.15 \text{ K} = T_2$$

$$c_{p3} = c_{p1} + \frac{c_{p2} - c_{p1}}{T_2 - T_1} (T - T_1) \left( \frac{\text{J}}{\text{kg} \cdot \text{K}} \right), \quad T > 923.15 \text{ K}$$

$$k = a + bT + cT^2 \left( \frac{W}{m \cdot K} \right)$$

$$a = 17.5 \cdot \left( \frac{1 - 2.23W_{Zr}}{1 + 1.61W_{Zr}} - 2.62W_{Pu} \right)$$

$$b = 1.54 \cdot 10^{-2} \cdot \left( \frac{1 + 0.061W_{Zr}}{1 + 1.61W_{Zr}} + 0.9W_{Pu} \right)$$

$$c = 9.38 \cdot 10^{-6} \cdot (1 - 2.7W_{Pu})$$

Irradiated UO2 (temperature in K):

$$k = k_0 \cdot F_1 \cdot F_2 \cdot F_3 \cdot F_4 \left( \frac{W}{m \cdot K} \right)$$

$$F_1 = \left( \frac{1.09}{Bu^{3.265}} + \frac{0.0643}{Bu^{0.5}} T^{0.5} \right) \arctan \left( \left( \frac{1.09}{Bu^{3.265}} + \frac{0.0643}{Bu^{0.5} T^{0.5}} \right)^{-1} \right)$$

$$F_2 = 1 + \frac{0.019Bu}{(3 - 0.019Bu)(1 + \exp(\frac{T - 1200}{-100}))}$$

$$F_3 = 1 - \frac{0.2}{1 + \exp(\frac{T - 900}{80})}$$

$$F_4 = 1 - 2.5P, \quad P < 0.1$$

$$F_4 = \frac{1 - P}{1 + 2P}, \quad P \geq 0.1$$

Irradiated MOX (temperature in K):

$$k = k_0 \cdot F_1 \cdot F_2 \cdot F_3 \cdot F_4 \left( \frac{W}{m \cdot K} \right)$$

$$F_1 = \left( \frac{1.09}{Bu^{3.265}} + \frac{0.0643}{Bu^{0.5}} T^{0.5} \right) \arctan \left( \left( \frac{1.09}{Bu^{3.265}} + \frac{0.0643}{Bu^{0.5} T^{0.5}} \right)^{-1} \right)$$

$$F_2 = 1 + \frac{0.019Bu}{(3 - 0.019Bu)(1 + \exp(\frac{T - 1200}{-100}))}$$

$$F_3 = 1 - \frac{0.2}{1 + \exp(\frac{T - 900}{80})}$$

$$F_4 = 1 - 2.5P, \quad P < 0.1$$

$$F_4 = \frac{1 - P}{1 + 2P}, \quad P \geq 0.1$$

## 6 Code Validation Efforts

SAM utilizes the application- and validation-driven code development approach. The code is being applied each year to selected demonstration or validation problems where the physics and scales of the problem may expand or increase with complexity in successive years. These validations lead up to the continuous assessment of the code capabilities and performance for a wide range of advanced reactor applications. Code validation activities in FY20 include using test data from the Fast Flux Test Facility (FFTF), the High Temperature Test Facility (HTTF), and several separate effects test facilities for pebble-bed modeling. A brief summary of these validation efforts is presented in this Section, while details have been summarized in earlier reports in FY20.

### 6.1 Code Validation using FFTF Test Data

The Fast Flux Test Facility (FFTF) was a 400 MW thermal powered, oxide-fueled, liquid sodium cooled test reactor, built to assist development and testing of advanced fuels and materials for fast breeder reactors. In July 1986, a series of unprotected Loss of Flow Without Scram (LOFWOS) transients were performed in FFTF as part of the Passive Safety Testing (PST) program. The LOFWOS Test #13, which was initiated at 50% power and 100% flow with the pump pony motors left off, has been chosen as a benchmark case by IAEA to support collaborative efforts within international partnerships on the validation of simulation tools and models in the area of sodium fast reactor passive safety in an IAEA Coordinated Research Project (CRP), launched in October 2018.

To participate the IAEA CRP and enhance the SAM validation base for advanced reactor transient safety analysis, benchmark simulations of the FFTF LOFWOS Test #13 are performed using the SAM code. In this first phase of the validation effort, the thermal-hydraulic behavior of the reactor system is the focus and the reactor kinetics is not considered in the SAM FFTF model. Instead, the results of Argonne's neutronics calculations are directly used, including the power shape of the active core region and the power history during the transient. The simulation results of FFTF at steady state agreed well with the measured data from the test. During the transient, reasonably good agreement was also obtained, including the mass flow rate of the primary loop, cold leg and hot leg temperature of primary and secondary loops. The maximum difference of temperature between model prediction and measurements is about 10 K, while the mass flow rate maximum difference is less than 5%. Future work to improve the model will focus on introducing the reactivity predictions into the model, as well as better understanding or resolving the current discrepancies with the measured data. The details of the SAM code validation using FFTF test data can be found in Ref. [30].

### 6.2 Code Validation using HTTF Test Data

The High Temperature Test Facility (HTTF) at Oregon State University was designed to examine the performance of High Temperature Gas-Cooled Reactors (HTGRs) during steady-state and transient operations. Previously, SAM has been used to model the thermal hydraulic behavior in the General Atomic's MHTGR design [31]. The test campaign at HTTF provides a valuable opportunity to utilize SAM to model an integral effect facility and to assess and improve its modeling approach – the ring model – of a prismatic block core MHTGR design. In this validation study, a similar ring model has been developed to simulate the HTTF with 50 concentric cylindrical rings which cover all in-vessel components as well as ex-vessel RCCS. Steady state calculations for full power were performed and the results agreed well with those obtained from RELAP5-3D

and STAR-CCM+. Benchmarking of the first major test – Test PG-26 – in HTTF was carried out. There were some unexpected challenges in the operation of the test and so it provides only limited validation value to compare SAM simulations with test data. Nevertheless, this initial benchmarking effort provides much insight as well as the needed setup for future benchmarking activities, particularly in mapping instrumentation locations to locations in the ring model. The details of the SAM code validation using HTTF test data can be found in Ref. [32].

### **6.3 Code Validation for pebble bed modeling**

To support system level safety analysis of HTGR and PB-FHR applications, correlations for effective thermal conductivity of pebble bed have been recently implemented in SAM. Currently, two correlations have been selected and implemented in SAM, i.e., the ZBS and IAEA [33] correlations. The High Temperature Test Unit (HTTU) facility, developed by the PBMR company in collaboration with the North-West University and M-Tech Industrial (Pty) Ltd. in South Africa, is an experiment facility dedicated to study the different thermal-fluid phenomena of pebble bed type of HTGR. A separate effect test has been performed to investigate the effective thermal conductivity of the pebble bed. Pebble surface temperatures are measured at multiple vertical and circumferential locations. These temperature measurements were used to derive the effectively thermal conductivity of the pebble bed based on the Fourier's law. Two test cases, namely the 82kW and 20kW cases, have been selected to validate SAM's implementation of effective thermal conductivity correlations. For the 82kW case, SAM-predicted temperatures using the IAEA and ZBS correlations agree pretty well with experimental data. For the 20kW case, the IAEA correlation produces slightly better prediction on pebble surface temperature, while the ZBS correlation produces higher temperatures than experiments. The details of the SAM code validation for pebble bed friction pressure drop can be found in Ref. [34].

Another study was performed to validate the capability of SAM to predict the frictional pressure drop through pebble beds. Selected experimental data were used for code validation, including data from test facilities at Texas A&M University, Missouri University of Science and Technology, and North-West University of South Africa. SAM implemented three empirical correlations to predict frictional pressure drop: the classical Ergun correlation; the KTA correlation, which is widely used in high-temperature gas-cooled reactor applications; and the Einfeld and Schnitzlein correlation, which explicitly considers the wall effect. Code validation was performed using all three correlations. For all selected experimental data, the KTA correlation shows the best performance and agrees very well with experimental measurement; the Einfeld and Schnitzlein correlation shows acceptable accuracy; the Ergun correlation, however, over-predicts frictional pressure drop for most selected data points. The details of the SAM code validation for pebble bed friction pressure drop can be found in Ref. [35].

## **Acknowledgement**

The SAM code development has been funded by multiple sources including several DOE programs (including NEAMS, GAIN, TCF, FOA), Argonne LDRD, and the U.S. Nuclear Regulatory Commission.

The SAM development, demonstration, and validation were greatly aided by additional efforts and inputs from a large number of colleagues, collaborators, and students, including: Aydin Karahan, Thanh Hua, Dan O’Grady, Travis Mui, Yang Liu, and Jim Jerden at Argonne National Laboratory; Haihua Zhao, Quan Zhou, Lambert Fick, Alex Heald at Kairos Power; Joseph Kelly and Steve Bajorek at U.S. Nuclear Regulatory Commission; Cody Permann, Alex Lindsay, and David Andrs at Idaho National Laboratory; Kazi Ahmed at University of Wisconsin.



## Reference:

- [1] Hu, R., SAM Theory Manual, Argonne National Laboratory, ANL/NE-17/4, March 2017.
- [2] Hu, R., L. Zou, G. Hu, SAM User's Guide, Argonne National Laboratory, ANL/NSE-19/18, Argonne, IL, August 2019.
- [3] Hu, R., "Three-Dimensional Flow Model Development for Thermal Mixing and Stratification Modeling in Reactor System Transient Analyses," *Nuclear Engineering and Design*, 345, 209-215 (2019).
- [4] Hu R. and Yu Y., "A Computationally Efficient Method for Full-Core Conjugate Heat Transfer Modeling of Sodium Fast Reactors," *Nuclear Engineering and Design*, Vol. 308, 182-193, (2016).
- [5] Ling Zou, Guojun Hu and Rui Hu. "Code Enhancement to SAM Multi-scale/multidimensional Heat Transfer Modeling Capabilities." American Nuclear Society Winter Meeting, Chicago, IL US, November 15-19, 2020.
- [6] Cody J. Permann, Derek R. Gaston, David Andrs, et al., MOOSE: Enabling massively parallel multiphysics simulation, *SoftwareX*, 11 (2020), 100430.
- [7] Ling Zou, Daniel Nunez, and Rui Hu, "Development and Validation of SAM Multi-dimensional Flow Model for Thermal Mixing and Stratification Modeling," Argonne National Laboratory, ANL-NSE-20/19, June 2020.
- [8] R. Scarlat, et al., NEUP Project #16-10647 Final Report: Experimental and Modeling Investigation of Overcooling Transients that include Freezing, in Fluoride-Salt Cooled High-Temperature Reactors (FHRs), University of California, UCBS-REC-2020-001, 2020.
- [9] Ling Zou, Guojun Hu and Rui Hu. "Code Enhancement to SAM Multi-scale/multidimensional Heat Transfer Modeling Capabilities." American Nuclear Society Winter Meeting, Chicago, IL, November 15-19, 2020.
- [10] Fang, J., L. Brockmeyer, G. Hu, L. Zou, R. Hu, Elia Merzari and K. Karazis. "Center of Excellence Collaboration Projects: Second Wave." Argonne National Laboratory, ANL/NSE-20/22, June 30, 2020.
- [11] Hu, Guojun, Daniel O'Grady, Ling Zou and Rui Hu. "Development of a Reference Model for Molten-Salt- Cooled Pebble-Bed Reactor Using SAM." Argonne National Laboratory, ANL/NSE-20/31, September 2020.
- [12] Feng, B., Y. Cao, A. Kasam-Griffith, L. Ibarra, D. Nunez, R. Hu, T. Hua and et al., unpublished information, Argonne National Laboratory, 2020.
- [13] Hu. G., Hu, R., Kelly, J. M., and Ortensi, J., Multi-Physics Simulations of Heat Pipe Micro Reactor, Argonne National Laboratory, ANL/NSE-19/25, 2019.
- [14] Hu G., Zhang G., Hu R., Reactivity Feedback Modeling in SAM, Argonne National Laboratory, ANL/NSE-19/1, February 2019.
- [15] American Nuclear Society, "American National Standard Decay Heat Power in Light Water Reactors," ANSI/ANS-5.1-2005, 2005.
- [16] G. Zhang and R. Hu, "Development of MSR Transient Safety Analysis Capability in SAM", 2018 American Nuclear Society Annual Meeting, Philadelphia PA, June 17 - 21, 2018.

- [17] Jerden J., "Molten Salt Thermophysical Properties Database Development: 2019 Update," ANL-CFCT-19-6, Argonne National Laboratory, 2019.
- [18] Compere E. L., Kirslis S.S., et al, "Fission Product Behavior in the Molten Salt Reactor Experiment," ORNL-4865, Oak Ridge National Laboratory, 1975.
- [19] OECD/NEA, Handbook on Lead-bismuth Eutectic Alloy and Lead Properties, Materials Compatibility, Thermalhydraulics and Technologies, Nuclear Science, OECD Publishing, Paris, 2015.
- [20] A. Banerjee et al., "High Temperature Heat Capacity of Alloy D9 Using Drop Calorimetry Based Enthalpy Increment Measurements," *International Journal of Thermophysics*, Vol. 28, No. 1, pp. 97-108, (2007).
- [21] L. Leibowitz et al., "Thermal Conductivity and Thermal Expansion of Stainless Steels D9 and HT9," *International Journal of Thermophysics*, Vol. 9, No. 5, pp. 873-883, (1988).
- [22] N. Yamanouchi et al., "Accumulation of Engineering Data for Practical Use of Reduced Activation Ferritic Steel: 8 % Cr-2%W-0.2%V-0.04%Ta-Fe," *Journal of Nuclear Materials*, Vol. 191, pp. 822-826, (1992).
- [23] A. Karahan, "Development of a Thermal Conductivity Model for the Irradiated U-Pu-Zr Metallic Fuels," *Trans. Am. Nucl. Soc.*, 117, pp. 563-566, (2017).
- [24] A. Karahan, "Modeling of Thermo-mechanical and Irradiation Behavior of Metallic and Oxide Fuels for Sodium Fast Reactors," Ph.D. Thesis, Massachusetts Institute of Technology, (2009).
- [25] H. Savage, "The Heat Content and Specific Heat of Some Metallic Fast-Reactor Fuels Containing Plutonium," *Journal of Nuclear Materials*, Vol. 25, pp. 249-259, (1968).
- [26] K. Maeda et al., "Change of Fuel-to-Cladding Gap Width with the Burn-up in FBR MOX Fuel Irradiated to High Burnup," *Journal of Nuclear Materials*, Vol. 327, pp. 1-10, (2004).
- [27] M. C. BILLONE, et al., "Status of Fuel Element Modeling Codes for Metallic Fuels," *Proc. ANS Intl. Conf. on Reliable Fuels for LMRs*, pp. 5.77-5.92, (1986).
- [28] S. G. Popov et al., "Thermophysical Properties of MOX and UO<sub>2</sub> Fuels Including the Effects of Irradiation," ORNL/TM-2000/351, Oak Ridge National Laboratory, (2000).
- [29] T. H. Fanning et al., "The SAS4A/SASSYS-1 Safety Analysis Code System. Chapter 8: DEFORM-4: Steady-State and Transient Pre-failure Pin Behavior," ANL/NE-16/19, Nuclear Engineering Division, Argonne National Laboratory, (2017).
- [30] Yang Liu and Rui Hu. "Benchmark Modeling and Simulation of the FFTF LOFWOS Test #13 Using SAM." Argonne National Laboratory, ANL/NSE-20/8, March 2020.
- [31] P. Vegendla, R. Hu and L. Zou, "Multi-Scale Modeling of Thermal-Fluid Phenomenon Related to Loss of Forced Circulation Transient in HTGRs," Argonne National Laboratory, ANL-19/35, September 2019.
- [32] Thanh Hua, Ling Zou, and Rui Hu, Simulations of the High Temperature Test Facility using SAM, Argonne National Laboratory, ANL/NSE-20/26, August 2020.
- [33] IAEA. Heat Transport and Afterheat Removal for Gas Cooled Reactors Under Accident Conditions. Technical report IAEA-TECDOC-1163, International Atomic Energy Agency, 2000.

- [34] Ling Zou and Rui Hu. "Recent SAM Code Improvement to Heat Transfer Modeling Capabilities." Argonne National Laboratory, ANL/NSE-19/46, December 2019.
- [35] Ling Zou and Rui Hu, SAM Code Validation on Frictional Pressure Drop through Pebble Beds, Argonne National Laboratory, ANL/NSE-20/5, March 2020





## **Nuclear Science and Engineering Division**

Argonne National Laboratory  
9700 South Cass Avenue, Bldg. 208  
Argonne, IL 60439

[www.anl.gov](http://www.anl.gov)



Argonne National Laboratory is a U.S. Department of Energy  
laboratory managed by UChicago Argonne, LLC